Investigation of the regional variability of the ice water content produced by supercooled stratiform clouds

Faculty of Physics and Earth Sciences
University of Leipzig

B A C H E L O R   T H E S I S

Franziska Hellmuth
Matriculation number 3277524

Supervisors:
Prof. Dr. A. Macke
Dr. habil. A. Ansmann

Leipzig, 26 January 2016

Abstract

Previous satellite based and ground-based remote-sensing studies indicate that heterogeneous freezing efficiency is latitudinal depending. Therefore, this study evaluates the relationship between cloud-top temperature and the amount of ice water content (IWC) produced in shallow mixed-phase clouds at North Slope of Alaska and Southern Great Plains. The analyses presented here are based on ground based measurements from the Atmospheric Radiation Measurement (ARM) program that were performed on a location in the Arctic and in the sub-tropics in 2014. A combination of lidar, radar, microwave radiometer and modelled temperature profiles were used to develop an algorithm to calculate the ice water content at the base of less than $300\,\mathrm{m}$ thick supercooled liquid cloud layers at each station. A process based on lidar and radar data defines cloud bases and tops of the supercooled liquid cloud layers. In an additional step the IWC $60\,\mathrm{m}$ below the detected cloud base is calculated.

The results agree with previous studies in such a way that the IWC increases with decreasing cloud top temperature in shallow, mixed-phase clouds. Furthermore, a peak in IWC is observed at North Slope of Alaska at cloud top temperatures between $-15\,^{\circ}\mathrm{C}$ and $-10\,^{\circ}\mathrm{C}$. The fact, that there is no peak observed in the Southern Great Plains leads to the conclusion that both instrumental or meteorological effects could influence the results of the IWC. Accurate instrument calibration and correction for atmospheric effects such as attenuation are required to cancel out possible instrumental effects on the derived cloud statistics.

Table of Contents

Chapter 1

Introduction

Clouds can basically be divided into three groups, according to the phase partitioning therein. They can appear either as pure liquid clouds, pure ice clouds, or as mixed-phase clouds which contain a mixture of ice and liquid water.

Mixed-phase clouds are specifically relevant because they contain a variable ratio of liquid water and ice. They occur at temperatures between approximately - 35 °C and 0 °C. In this temperature range, ice formation is initialized heterogeneously on the surface of aerosol particles acting as ice nucleating particles (INP). Amongst other aerosol types biogenic aerosols and dust particles are efficient and an important source for ice [*Hoose and Möhler* [2012]].

Depending on the ratio of liquid and ice, a mixed-phase clouds may either warm or cool the Earth's surface. Heterogeneous ice formation influences the atmospheric radiative transfer [*Sun and Shine* [1994]] and the production of precipitation [*Mülmenstädt et al.* [2015]].

The knowledge of mixed phases clouds is important for radar, lidar, satellite retrievals, radiative transfer and climate models [*Korolev et al.* [2003]].

Mixed-phase clouds appear manifold in the atmosphere, either as deep precipitation systems or as shallow cloud layers. Even though precipitation systems are most relevant for the hydrological cycle, they are difficult to study because of the large amount of processes occurring therein. Key to understand the relationship between atmospheric thermodynamics and aerosol conditions on mixed-phase cloud properties are shallow cloud layers such as altocumulus, altostratus or stratocumulus clouds.

Shallow mixed phase cloud layers were used previously to study the dynamic of aerosol-cloud interaction under ambient conditions. These cloud types are particularly well fitted for process studies. Mixed phase clouds show strict limits on basic environmental variables such as temperature, pressure and humidity. As an added benefit, these shallow cloud layers can be easily observed by cloud radars and lidars. Inside deep precipitating clouds the signal will be massively attenuated and the turbulences are strong and therefore it is impossible for lidar to penetrate through deep convective clouds and for Cloud-Doppler radar to collect valuable information on particle fall velocities. For climate research, shallow cloud layers are also important because of the difficulty to forecast their impact on the Earth's radiation budget.

Even though shallow mixed-phase clouds are relatively easy to analyse, it is still difficult to understand their role in the radiation budget of the Earth.

TROPOS has already conducted a series of studies on the role of desert dust on heterogeneous ice formation [*Ansmann et al.* [2009],*Seifert et al.* [2010]]. The impact of volcanic ash was investigated by *Seifert et al.* [2011]. *Seifert et al.* [2010] also found a difference in heterogeneous freezing efficiency under dust-laden and dust-free conditions at Cape Verde and Leipzig. *Kanitz et al.* [2011] observed a north-south decrease in the efficiency of heterogeneous freezing by comparing measurements from Punta Arenas (53 °S), Chile, Stellenbosch (34 °S, near Cape Town), South Africa, three north-south cruises with the research vessel *Polarstern* and Leipzig (51 °N), Germany. Furthermore *Seifert et al.* [2015] published a statistical analysis on the occurrence of heterogeneous ice formation in stratiform cloud layers over the Amazon Basin (2.3 °S, 60 °N, near Manaus), Brazil. There is a possibility of seasonal variations on the efficiency of heterogeneous ice formation in the Amazon Basin region. Based on a retrieval of combined measurements of cloud radar and lidar, *Bühl et al.* [2013] quantified the amount of ice formed in shallow mixed-phase clouds for the site of Leipzig. This approach was recently extended by *Bühl et al.* [2016] who presents a detailed analysis of the quantitative ice formation at Leipzig.

Ground-based measurements can only be preformed during short time periods or in specific regions, with satellites measurements globally over long time periods. From observations of the space-borne Cloud-Aerosol Lidar and Infrared Pathfinder Satellite Observation (CALIPSO) lidar and CloudSat radar *Zhang et al.* [2010] has found seasonal and regional differences in the properties of mid-level, shallow, mixed-phase clouds. The study from *Zhang et al.* [2010] resulted in a seasonal day-night-variation at different latitudes. In a further 4-year study it was examined that dust is affecting the ice formation in mid-level, supercooled, stratiformed cloud layers [*Zhang et al.* [2012]].

It raises the question if regional differences in ice formation efficiency, as it was reported by *Kanitz et al.* [2011], *Seifert et al.* [2010], and *Zhang et al.* [2010], [2012], also affect the regional relation between temperature and ice water content produced by shallow mixed-phase cloud layers. So far only datasets from mid-latitudes were collected and analysed by TROPOS studies. In turn, the studies based on the space-borne observations of CALIPSO and CloudSat suffer of high detection thresholds [*Bühl et al.* [2016]]. Weak signals as they are produced by small amounts of ice in most mixed-phase clouds at temperatures above - 10°C remain undetected when observed from the large distances of the satellite sensors.

This work presents a study of data collected within the Atmospheric Radiation Measurement (ARM) program at sites in the Arctic and the sub-tropics to investigate the latitudinal variability of the ice water content (IWC) in shallow, mixed-phase clouds. Another investigation shows if other factors, such as statistical effects or instrument effects allow a comparison between different stations.

This study is based on a similar approach as presented by *Bühl et al.* [2013] and *Bühl et al.* [2016]. The purpose of this study is to check whether the average ice water content varies depending on the cloud top temperature in different regions, namely at North Slope of

Alaska (NSA) and Southern Great plains (SGP), by using combined measurements of lidar, cloud radar and microwave radiometer. To accomplish that goal, a retrieval algorithm was developed that derives the required subset of shallow mixed-phase clouds from the continuous long-term datasets.

The instruments and their location that were used in this study are presented in Chapter 2. The lidar / radar cloud detection algorithm, that was developed and realized within this study, is presented in Chapter 3, summarized results from this study are presented in Chapter 4, and discussed in Chapter 5.

Chapter 2

Locations, Instruments and Dataset

This work is based on the analysis of datasets collected at sites of the Atmospheric Radiation Measurement (ARM) program. If not otherwise stated, the ARM website is used as reference for the content presented within this section [*ARM* [2015a]].

The ARM Program was built in 1989 by the US Department of Energy with the purpose of studying the global climate change. Several ground based instruments have been installed to study cloud formation processes and the influence on the global radiative transfer. As the program evolved, further measurements for aerosol and precipitation were added. The ground sites have been extended by three mobile facilities and an aerial facility. Since 1993, air measurements are an inherent part of the program. All data obtained by the facility are monitored for quality and made publicly accessible.

To represent a wide range of weather conditions and to obtain useful climate data, in the beginning three main sites were selected. The Southern Great Plains (SGP) site in Oklahoma, USA, was built in 1992, the location is the world's largest outdoor laboratory and covers the largest range of collected data sets. The site offers a wide variability of climate types and surface flux properties and a large seasonal change in temperature and humidity.

As the Arctic has been identified as a region sensitive to climate change, the ARM program established a station at North Slope of Alaska (NSA) in 1997. The station provides data on clouds and radiation processes at higher latitudes.

The site at Tropical Western Pacific was installed in a region with the warmest sea surface temperatures and widespread convective clouds, which play an important role in the annual variability in the global climate system. The station was built in 1996 and closed 2014.

One aim of ARM is the continuous vertical profiling of the atmospheric structure. For this study the main ARM sites data from NSA and SGP are used. A more detailed description of the purpose of these stations is presented in Section 2.1. All ARM sites operate a set of partially different types of remote sensing equipment. In general, every site operates at least one lidar system, one microwave radiometer and one cloud radar. Which instruments were used for the present study will be described in Section 2.2.

The set of instruments and the various locations of the ARM sites makes them fulfil the purpose of this study to inter-compare the regional differences in ice water content.

Figure 2.1: Map indicating NSA and SGP as measurement sites that provided the data for this study, while the Leipzig station is used as a reference to see the two stations in comparison on the world map. Adopted from *Wikimedia* [2015].

.

2.1 Locations

For this study the data from the two ARM super sites installed at NSA and at SGP were used to compare the variability of the IWC in dependence of the latitude.

Figures 2.1 and 2.2 present the location of the ARM super sites used within this study. As a reference the location of Leipzig is indicated as well in Figure 2.1. The data from the higher latitudes are of major interests for the refinement of model parameterizations for the Arctic. An additional goal is to improve the understanding of the interactions between the air-ocean-climate system. Furthermore, the simultaneous observation of ice and snow, water vapour, ocean currents and processes in the atmosphere over both land and sea will help to understand climate changes at higher latitudes.

Data on clouds and radiation processes in the higher latitudes are made available from the Station at North Slope of Alaska (see Figure 2.2). The main instruments were installed near Barrow (71° 19' 23.73" N, 156° 36' 56.70" W; Figure 2.3 left) in 1997 to characterize the vertical structure of the atmosphere.

In the Arctic climate, around NSA, ice and snow contribute to a large extent to the total mass of clouds and precipitation, even though absolute values are rather low. Thus, small changes in the absolute amount of water vapour, ice, or liquid water or their ratio will strongly impact the radiation budget of the Arctic [*Nakamura and Oort* [1988]; *Zhang et al.* [1997]; *Stamnes et al.* [1999]]. In addition, the main strings of the global ocean currents are located at higher latitudes. There are reasons that these strands respond to climate-induced

Figure 2.2: Map indicating the research site in Barrow Alaska [*Icestories* [2015]].

changes. To understand that coupling between sea and air, atmospheric processes over sea and land must be characterized and integrated into global climate models. As the second station besides NSA, the ARM site Southern Great Plains (SGP) is used in the evaluation of regional differences in the ice water content (see Figure 2.1). The SGP site was the first field monitoring station, which was established by the ARM program. A large network of weather and climate research and instrumentation already existed before the site became an official ARM site. The first measurements at SGP started in 1992. In the following years, instruments were gradually added and therefore additional data could be processed.

The site was selected as the first ARM field measuring station, since it has a relatively homogeneous geography and a good accessibility. In addition, the temperature and specific humidity varies greatly seasonally. This makes the SGP site suitable for the observations of a broad range of atmospheric processes, such as boundary layer development, convective summer storms, or winter blizzards.

The SGP site consists of in-situ and remote sensing instruments (see Figure 2.3), which are clustered on a $143.000 \, \text{km}^2$ area in north-central Oklahoma, USA. Most of the instruments are in the central facility south-east of Lamont, Oklahoma (36° 36' 18,00" N, 97° 29' 6.00" W). They automatically gather data from surface and atmospheric properties. Overall, more than 30 groups of instruments are clustered at the SGP site.

The two ARM sites at SGP and NSA sufficiently fulfil the requirements for the study presented in this work. First, the instrumental basis at both sites is the same, as will be shown in Section 2.2. Second, atmospheric conditions between both sites differ strongly. Whereas Arctic conditions are present at NSA, subtropical to mid-latitudinal climate dominates at

Figure 2.3: Photographs of the field sites at NSA (left) and SGP(right) with parts of the instrumentation. Pictures taken from *ARM* [2015b] and *ARM* [2015c].

SGP. Third, aerosol conditions vary strongly between both sites, which could potentially effect heterogeneous ice formation efficiency in the observed mixed-phase clouds. For SGP, *Michalsky et al.* [2010] reports average aerosol optical depths of 0.15 at a wavelength of 500 nm. For NSA, *Yin and Min* [2014] report respective mean aerosol optical depths of 0.05. This suggests, that the aerosol load is increased at all heights at SGP compared to NSA. It should be noted, that the actual vertical aerosol profiling for both sites was not investigated in the scope of this work.

2.2 Instruments and Data

As described in Chapter 1, the goal of this thesis is to develop and apply an algorithm to characterize the ice water content of a defined subset of clouds, namely shallow mixed-phase clouds, based on ground-based remote observations, similar as it was done by *Bühl et al.* [2013] and *Bühl et al.* [2016]. Key to realize such an approach is the combination of lidar, cloud radar and microwave radiometer. Suites of these three instruments demonstrated well their applicability in the continuous observation and categorization of the vertical structure of clouds and aerosol [*Illingworth et al.* [2007]; *Shupe* [2007]]. All required instruments are available at the ARM sites and will be explained in more detail below. The cloud analysis algorithm will be explained in Chapter 3.
Table 2.1 lists the characteristics of the active remote sensing systems at the measurement sites.

CEIL - Ceilometer

A ceilometer is in general designed to measure the backscatter signals by aerosols and clouds, from which it derives the cloud base altitude. Lidar, the acronym for light detection and ranging is based on the emission of a laser pulse and the subsequent detection of the echo returned from targets. The distance, or range is found from the time it takes for the laser

Instrument	Wavelength / frequency	Temporal / spatial resolution	max. vertical range	Measured / derived quantity
KAZR	35 GHz	4 sec, 30 m	17.5 km	Reflectivity, copolar [dBZ]
MWR	23.8 GHz and 31.4 GHz	20 sec, column integrated	–	LWP [cm], wet window
HSRL		30 sec, 30 m	19.9 km	Particulate backscatter [$sr^{-1}\,m^{-1}$]
CEIL		16 sec, 30 m	7.5 km	backscatter [$sr^{-1}\,m^{-1}$]
GDAS		3 hours, 23 levels between 1000 and 20 hPa	27.1 km	Temperature [K]

Table 2.1: Characteristics of the instruments of the ARM - Climate research facility sites (North Slope of Alaska and Southern Great Plains), used in this study. Also the characteristics for the dataset from the Air Research Facility GDAS.

pulse to travel through the atmosphere to the target and back. Clouds and dust particles scatter the laser radiation; therefore, it is easy to determine the distance to the clouds with lidar.

Ceilometer provides the calibrated attenuated backscatter coefficient. This parameter is required also by the synergistic retrieval schemes of *Illingworth et al.* [2007] and *Shupe* [2007]. It provides a measure of particle backscattering that is corrected for instabilities of the instrumental setup but it is still subject to effects produced by attenuation caused by air molecules and particles.

The model CL31 (see Figure 2.4a), found at the ARM Stations has a maximal vertical range of 7.5 km.

KAZR - Ka-band ARM zenith radar

Lidar is generally sensitive to detect clouds in the troposphere, but can not penetrate thicker clouds [*Wang and Sassen* [2001], *Seifert et al.* [2010], *Bühl et al.* [2013]]. Therefore, usually Ka-band (35 GHz) or W-band (94 GHz) radars are used to characterize clouds at ranges where the lidar signal is attenuated. In general, the principle of radar measurements is based on an electromagnetic wave which is emitted from the radar transmitter and while the pulse propagates through the atmosphere the radiation interacts with objects that reflects a fraction of the pulse energy back to the receiver of the radar. The detected echo provides information about the target such as the reflectivity and its velocity along the line of sight of the radar. The distance to the target is found from the time the electromagnetic wave needs to travel from the emitter to the target and back [*Peters and Görsdorf* [2011]].

The KAZR zenith-pointing Doppler radar measures at a frequency of approximately 35 GHz (see Figure 2.4b), it measures the energy that is returned from each interval and thus enabling the detection of the Doppler spectrum. Cloud radars in general, determine the three Doppler moments, that are reflectivity, vertical velocity and spectral width. The temporal and spatial resolution of the KAZR is 4 seconds and 30 m, respectively.

Within this study, only the reflectivity parameter is used, that is determined by the meteorological radar range equation, which is listed in the handbook for KAZR [*Widener et al.* [2012]].

MWR - Microwave radiometer

A microwave radiometer measures the thermal radiation of the atmosphere. Atmospheric properties such as liquid water or ice crystals can be determined due to a certain range of the emission of microwave radiation. To estimate the atmospheric liquid water content, the knowledge about the total water amount in a column is needed. The total emissivity of the atmosphere depends on the total water amount in a column [*TROPOS* [2015]].

The MWR installed at the ARM sites provide the path-integrated amount of water vapour and liquid water (see Figure 2.4c). The microwave radiometer detects simultaneous emissions of water vapour and liquid water at 23.8 GHz and 31.4 GHz, respectively, along a path. From radiance measurements the integrated water vapour and liquid water path is calculated [*Liljegren et al.* [2001]]. More information to the MWR can be found in the MWR handbook [*Morris* [2006]].

GDAS1 - Global Data Assimilation System

Temperature information is required for the presented study in order to characterize the observed ice formation. Normally at NSA and at SGP radiosondes are launched twice a day. Because of the scarce temporal coverage and existing data gaps, it was decided to use data from GDAS1, which is a dataset that is based on the archived data from the Global Data Assimilation System (GDAS), *Oceanic and Administration* [2015].

The GDAS-model is based on measurements of ground-based, radiosonde, and satellite data. The horizontal resolution of the data is 1° x 1°, resulting in a resolution of 14.5 km x 89.4 km at SGP and of 101.7 km x 35.7 km at NSA. Profiles of the main atmospheric parameters are provided every 3 hours for 25 pressure levels between the ground and approximately 20 km height.

GDAS1 records have already been used in previous TROPOS studies, e.g., of *Seifert et al.* [2010], *Kanitz et al.* [2011] and *Seifert et al.* [2015].

HSRL - High spectral resolution lidar

To determine the actual particle backscatter coefficient, the high spectral resolution lidar method is applied at some of the ARM sites, such as at NSA. The HSRL uses the method of dividing the light in the part that is scattered from particles, molecules and light [*TROPOS*

[2015]]. The advantage of the HSRL is the particle backscatter coefficient is calculated directly. With increasing distance of the laser beam from the lidar the particle backscatter coefficient increases compared to the attenuated backscatter. Accordingly, attenuation of the signal by scattering and absorption processes are corrected.

At the ARM station in Barrow the HSRL measures the optical depth of aerosols, the volume backscatter coefficient, cross section, and depolarization (see Figure 2.4d). For this study only the backscatter coefficient of clouds is needed. Detailed information about the calibration of the instrument is available in the handbook on the ARM website [ARM [2015a]].

Since HSRL is only available at NSA the the inter-comparison of the ice water content between NSA and SGP is based on the ceilometer instead of the HSRL. In the results, in Chapter 4, also the calculated IWC for NSA based on a cloud retrieval that used HSRL data will be presented.

(a)

(b)

(c)

(d)

Figure 2.4: Instruments used for the analysis of the cloud datasets at SGP and NSA [*ARM* [2015a]]. (a) - (c) CEIL, KAZR and MWR, respectively. (d) shows the HSRL which is additionally used for the statistical comparison at NSA.

Chapter 3

Methodology

This chapter describes the data analysis process, that was developed and realized in the scope of this study, to determine the ice water content of mixed-phase clouds. The determination of required parameters from the four measuring instruments, radar, lidar, microwave radiometer, and the GDAS1 dataset will be explained.

The purpose of this study is to retrieve an algorithm to analyse a continuous long-term dataset for profiles which contain single-layer shallow mixed-phase clouds. With this retrieval the ice mass production in these clouds can be characterized and analysed.

Using radar and lidar, cloud tops and bases were defined. Furthermore, the cloud parameters temperature and reflectivity have been determined. The reflectivity and temperature is especially important for the calculation of the ice water content by the formula of *Hogan et al.* [2006] (see Section 3.2.3).

Basically, within this study a similar approach as in *Bühl et al.* [2013] and *Bühl et al.* [2016] is applied. The concept of *Bühl et al.* [2016] is based on the automatic Cloudnet algorithm [*Illingworth et al.* [2007]] that uses different remote sensing instruments, which are scaled to the same resolution as the cloud radar to obtain a height- and time-resolved mask of the observed particle types. For the study from *Bühl et al.* [2016] an automated algorithm was developed, which can be considered as a classification product for Cloudnet. As next step the physical state of the atmosphere at all altitude bins is classified into different categories, e.g. if the cloud contains liquid droplets or ice particles, or both.

In the study of *Bühl et al.* [2016], individual 30 second profiles were analysed to search for liquid water in a cloud. If liquid water is found, then the base and the upper level of the liquid water layer are stored. Below this height range of the liquid water layer an algorithm will search for ice particles. If below an ice particle is found, then the height between liquid and ice transfer is stored. This procedure is performed for all the profiles, afterwards a look for neighbouring profiles connected it to a cloud layer, only if they are within a temporal and vertical resolution of 300 seconds and 350 m, respectively. It is assumed that the driving micro-physics of a merged cloud layer are similar in the entire cloud layer. For statistical analysis, a cloud has to fulfil certain quality criteria: a coherent cloud structure for more than 20 minutes and without cloud seeding from higher-lying clouds for at least 85% of the
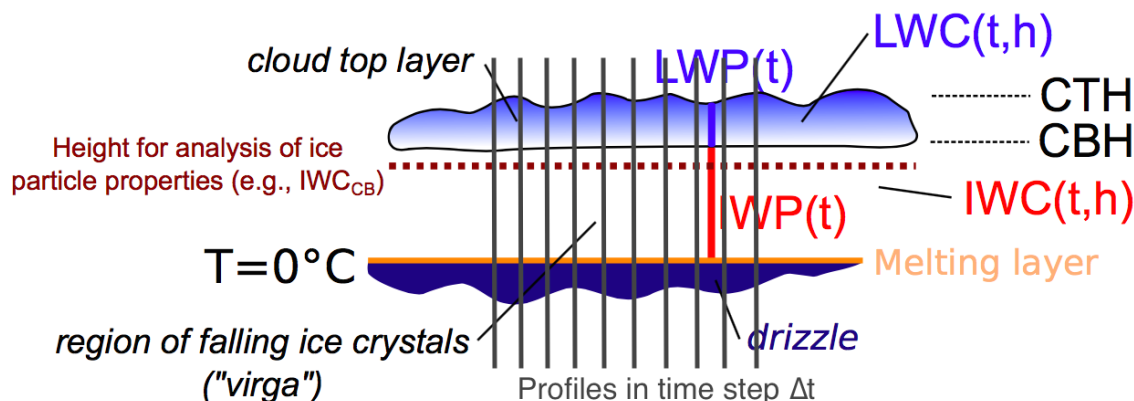
Figure 3.1: Scheme adapted from *Bühl et al.* [2016]. In this study the detection is made by each profile this is indicated by the vertical black lines. It represents the mixed-phase cloud layer. The liquid cloud bases are detected by the ceilometer, cloud tops by the KAZR.

cloud during the entire performance period, a liquid, or mixed phases cloud top has to be present. The properties of the detected clouds, for example, cloud top height, geometrical cloud thickness, standard deviation of the cloud height, cloud top height temperature, radar reflectivity, ice water content, liquid water content, LDR, lidar backscatter coefficient and lidar volume linear depolarization ratio are stored for further analysis. Figure 3.1 gives an overview of the various properties that were derived by the scheme of *Bühl et al.* [2016] for a cloud case. The picture also shows that some data was taken from an altitude of 60 m below the mixed phase cloud base (red dashed line below the cloud top layer). At this point, cloud droplets are absent and ice particles should still be largely unaltered by evaporation or aggregation processes. Therefore, their size and shape should be only connected to processes that have taken place within the mixed-phase cloud top layer. After the cloud has been identified, the cloud classification scheme from *Bühl et al.* [2013] was used to distinguish between liquid and mixed-phase cloud virgae, by taking into account additional selection criteria. From all cloud profiles the information is taken to make a decision between the micro-physical states of liquid or mixed-phase.

The Cloudnet retrievals required by the approaches of *Bühl et al.* [2013] and *Bühl et al.* [2016] are not available yet for the ARM sites. Thus, it was decided to implement a similar scheme as discussed by *Bühl et al.* [2016] to investigate qualitative differences in the ice water content formed in clouds at SGP and NSA.

The scheme developed within this work basically performs a simple target classification and provides profile-based statistics. Thus, the single profiles were not merged to coherent cloud layers. This approach is indicated in the adapted Figure 3.1 by the vertical black lines. A scheme for processing relevant data to calculate the ice water content is presented in Figure 3.2. This figure helps to explain how the data processing is done step by step. The data from CEIL, MWR and GDAS1 were interpolated to the reference instrument KAZR, which has a temporal and spatial resolution of 4 seconds and 30 m, respectively. Because the ceilo-
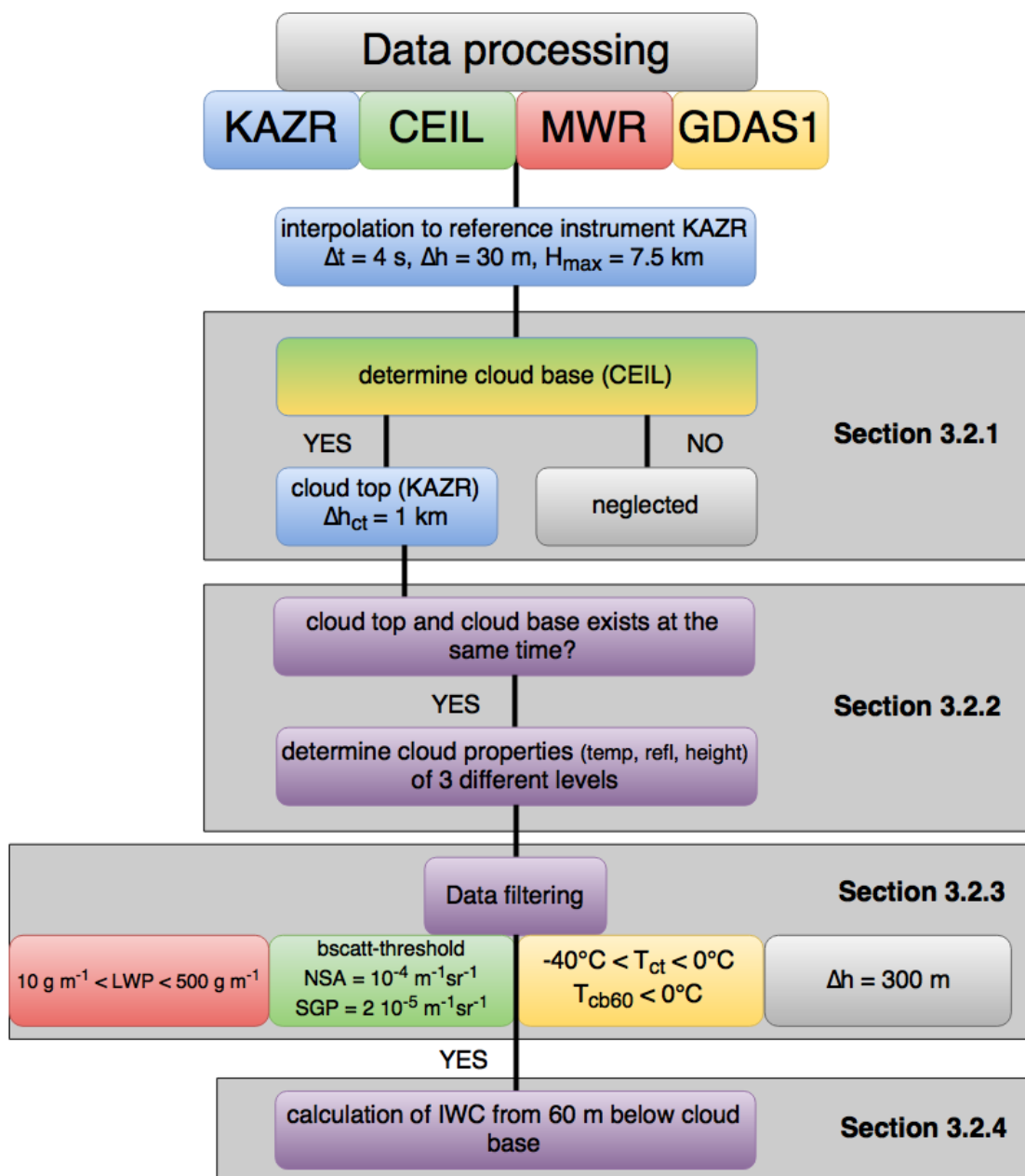
Figure 3.2: Overview of the steps required for data analysis to determine the ice water content at NSA and SGP for 2014.

meter has only a maximum detection height up to $7.5\,\mathrm{km}$, all values above $7.5\,\mathrm{km}$ were cut off and neglected. In the next step, cloud base and top heights and corresponding values of temperature and radar reflectivity are determined. Based on these values, the ice water content produced in mid-level clouds at SGP and NSA, was derived.

In the following, the data analysis scheme realized within this work is presented and applied to a 24-hour case study. First, the overview on the case study is given in Section 3.1. After

the unfiltered data were presented, the algorithm for calculating the IWC is explained in detail in Section 3.2. Section 3.2.1 shows the determination of the cloud base and cloud top and associated cloud parameters with the help of lidar and radar data. Section 3.2.2 demonstrates the filtering of the data to obtain only valid cloud profiles. In Section 3.2.3 the definition and calculation of the IWC is closer illustrated and explained.

3.1 Original Dataset: NSA on 6 August 2014

This section introduces the raw remote sensing measurements at NSA for 6 August 2014 as they were obtained from the ARM archive [*ARM* [2015a]] and the GDAS1 archive. This 24-hour case-day gives an example to determine cloud bases of mixed phases clouds and the cloud tops by using measurements from lidar and radar. The MWR helps to determine and classify certain clouds with liquid water content.

Figure 3.3 shows the 24-hour measurements of attenuated backscatter coefficient, radar reflectivity, liquid water path, and temperature. In the ceilometer data of 6 August 2014 at NSA, shown in Figure 3.3a, multiple cloud layers can be seen in the time-height cross-section of the attenuated backscatter coefficient. These are characterized by strong attenuated backscatter coefficients as they were observed during most of the measurement time at heights below 1 km. In addition, a rather weakly scattering cloud layer was observed between 3 km and 5 km height from 3 UTC to 9 UTC and strongly backscattering lofted cloud layers occurred in the second half of the day at various heights between 2 km and 5 km. Because the lidar signal is attenuated quickly in most of the observed cloud layers and the background noise is high, no conclusions on the vertical extent of the cloud layers nor on the possible existence of faint ice virgae can be drawn based on the ceilometer data.

Figure 3.3b shows the KAZR measurement. In a previous step, the KAZR data had to be filtered for noise artefacts as is explained in Eq. (4) in *Ewald et al.* [2015]. In comparison to the ceilometer measurement, the KAZR observation presents a complementary picture of the atmospheric structure. Background noise is weak, so that 4 different cloud layers are visible in the measurement. Weak reflectivity is observed close to the ground, indicating either ice or liquid fog particles. A cirrus cloud extends from 2 - 10 km height between 2 UTC and 9 UTC, producing weak precipitation at around 9 UTC.

The two thin layers at heights above 2 km between 14 UTC and 24 UTC producing high attenuated backscatter coefficients in the ceilometer measurement (Figure 3.3a) appear in the KAZR measurements as much thicker but weakly scattered cloud layers. This indicates that either ice crystals of drizzle precipitates from the liquid layers observed with the ceilometer. From Figure 3.3c it can be seen that the liquid water path (LWP) observed with the MWR is constantly around $50 \, \mathrm{g \, m^{-2}}$ until 14 UTC. This indicates that the fog observed with CEIL and KAZR contains liquid water droplets or at least a mixture of ice and liquid water. After 14 UTC, the LWP increases to values around $150 \, \mathrm{g \, m^{-2}}$. Thus, the cloud layers observed in the middle troposphere are either drizzling warm clouds or mixed-phase clouds.

A more-detailed view on the temperature profiles is given in Figure 3.4. Nevertheless, from
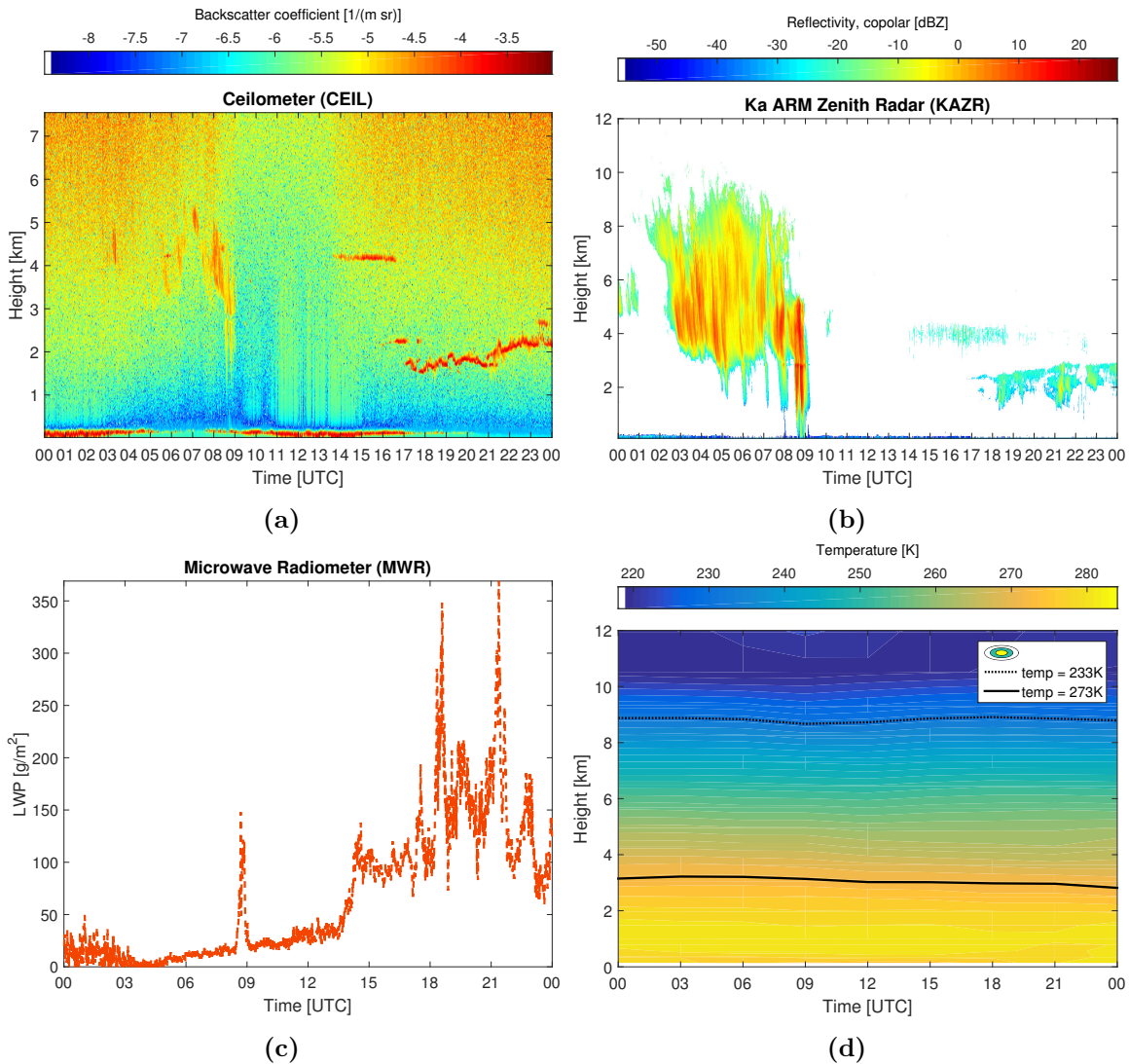
Figure 3.3: Original data provided by the ARM website on 6 August 2014. In a) backscatter coefficient of ceilometer, b) radar reflectivity corrected with the *Ewald et al.* [2015] algorithm, c) liquid water path from MWR, d) temperature profile of the GDAS1 data. Note that the vertical resolution is different for a), b) and d), where in a) it is to the maximum range of 7.5 km and b), d) is only up to 12 km altitude.

the location of the - 40°C and 0°C isotherms it can be seen that the fog layers at below 1 km height as well as the low cloud layer observed in the afternoon at around 2.5 km height are pure liquid clouds, producing drizzle to some extent as shown in the KAZR measurement. The geometrically deep cloud system observed in the morning reaches up to the - 40°C isotherm, thus it is likely that it is a cirrus cloud consisting entirely of ice crystals. Only the cloud layer observed from 14 UTC to 18 UTC at around 4 km height is likely to be a mixed-phase cloud producing slight amounts of ice precipitation as is indicated by the virgae

observed with KAZR (Figure 3.3b).

3.2 Cloud detection and classification

In the first analysis step, the original data of CEIL, MWR and GDAS1 shown in Figure 3.3 was interpolated onto the time-height grid of 4 seconds and 30 m, respectively, of KAZR. Based on this homogenized dataset, cloud bases and cloud tops of observed liquid layers can be determined as will be explained in the following subsection.

3.2.1 Cloud base and top heights

First, the cloud base and top heights of all liquid layers needs to be defined. This processing step is based on data from CEIL and KAZR. Since the lidar can not penetrate through thick clouds a combination of lidar and radar is used. Hereby, the lidar is used to derive the cloud base height whereas radar data is used to derive the cloud top height.

As a first step, the height of the cloud base (H_{cb}) is determined for each profile. For this purpose, the attenuated backscatter coefficient from the ceilometer dataset of 6th August 2014 is presented in Figure 3.5. It should be noted that at NSA, a backscatter coefficient threshold of $10^{-4}\,\mathrm{m}^{-1}\,\mathrm{sr}^{-1}$ was used and in SGP a threshold of $2 \cdot 10^{-5}\,\mathrm{m}^{-1}\,\mathrm{sr}^{-1}$, similar to the one used for Cloudnet [*Illingworth et al.* [2007]]. In the selection of the two threshold values of the attenuated backscatter for NSA and SGP it was considered that mixed-phase clouds at NSA usually occur at much lower heights than at the subtropical site of SGP. Thus, attenuation of the lidar signal is stronger at SGP than at NSA because the laser pulse needs to penetrate a larger column of air, clouds and aerosols. For this study the thresholds were therefore adjusted in such a way that the number of false-positive detections of liquid cloud layers at - 40 °C to 0 °C was minimal.

The first height level at which the attenuated backscatter coefficient is greater than the threshold is defined as the cloud base height. Furthermore, backscatter coefficients, which are less than zero are neglected because they are physically undefined.

In Figure 3.5, the interpolated attenuated backscatter coefficient from CEIL is shown. In a) is the height range up to the maximum detection altitude of 7.5 km, b) shows in addition to the interpolated backscatter coefficient the detected altitude of the cloud bases indicated as black X, up to an altitude of 6 km. The values of the attenuated backscatter coefficient in the presence of a cloud is roughly above $10^{-4}\,\mathrm{m}^{-1}\,\mathrm{sr}^{-1}$. It is remarkable that no liquid cloud bases were detected in the deep cloud observed in the morning of the case study. This is a further indication that the cloud consisted entirely of ice crystals that in general produce attenuated backscatter coefficients that are lower than those caused by cloud droplets. A few cloud bases are rarely observed in 4 km at 3 UTC and 6 UTC. Between 5 UTC and 8 UTC no cloud base is detected in the boundary layer, it can be assumed that the backscatter signal is too weak to be recognized as cloud base. It is possible based on the data of CEIL to identify multiple cloud bases. This is recognized in the period from 16 UTC to 18 UTC, when cloud base heights where detected in the boundary layer, at approximately 1.5 km height, at
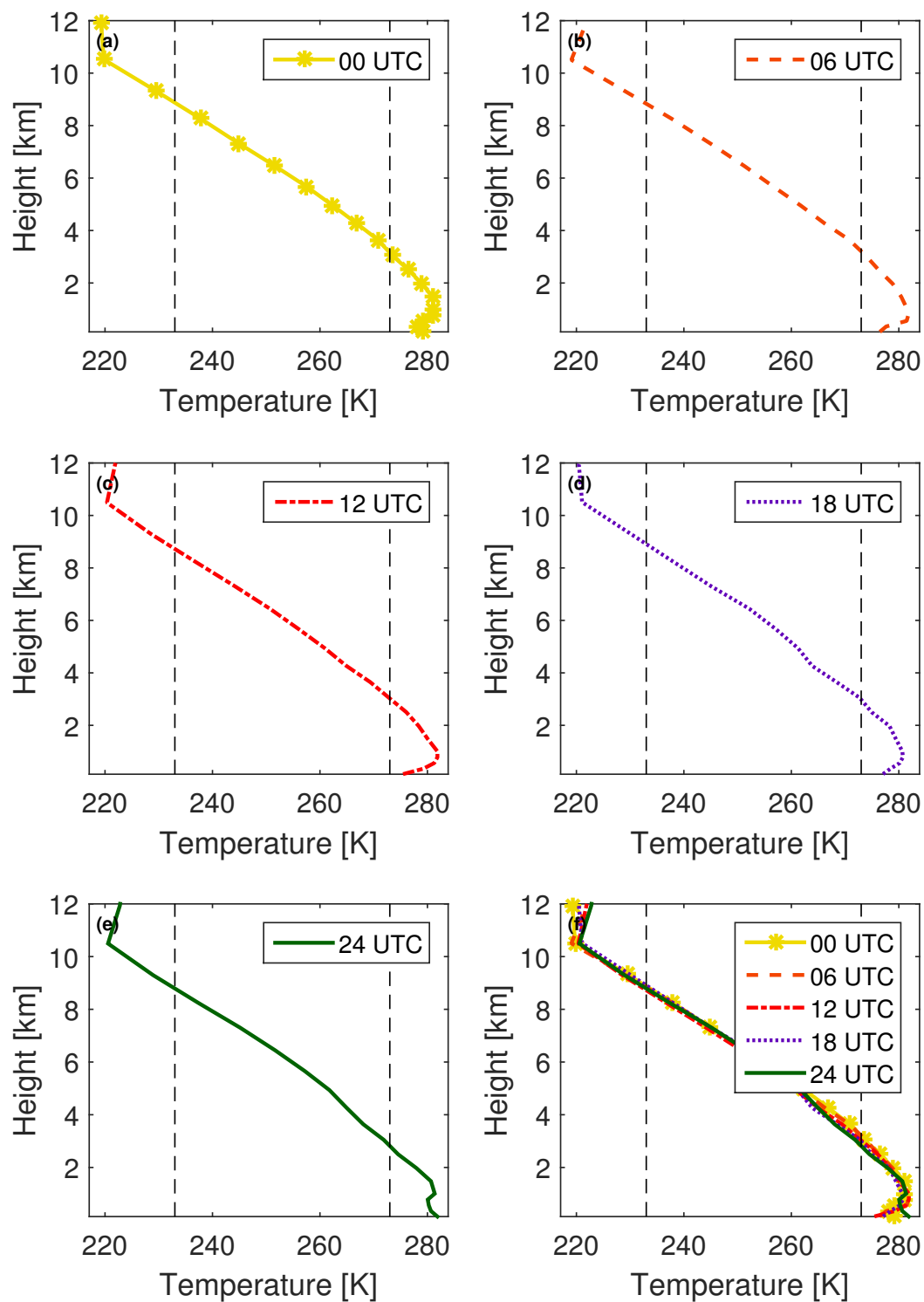
Figure 3.4: GDAS1 profiles from 00, 06, 12, 18 and 24 UTC for the 6th August 2014. In (f) all profiles are printed in one plot to show the similarity.
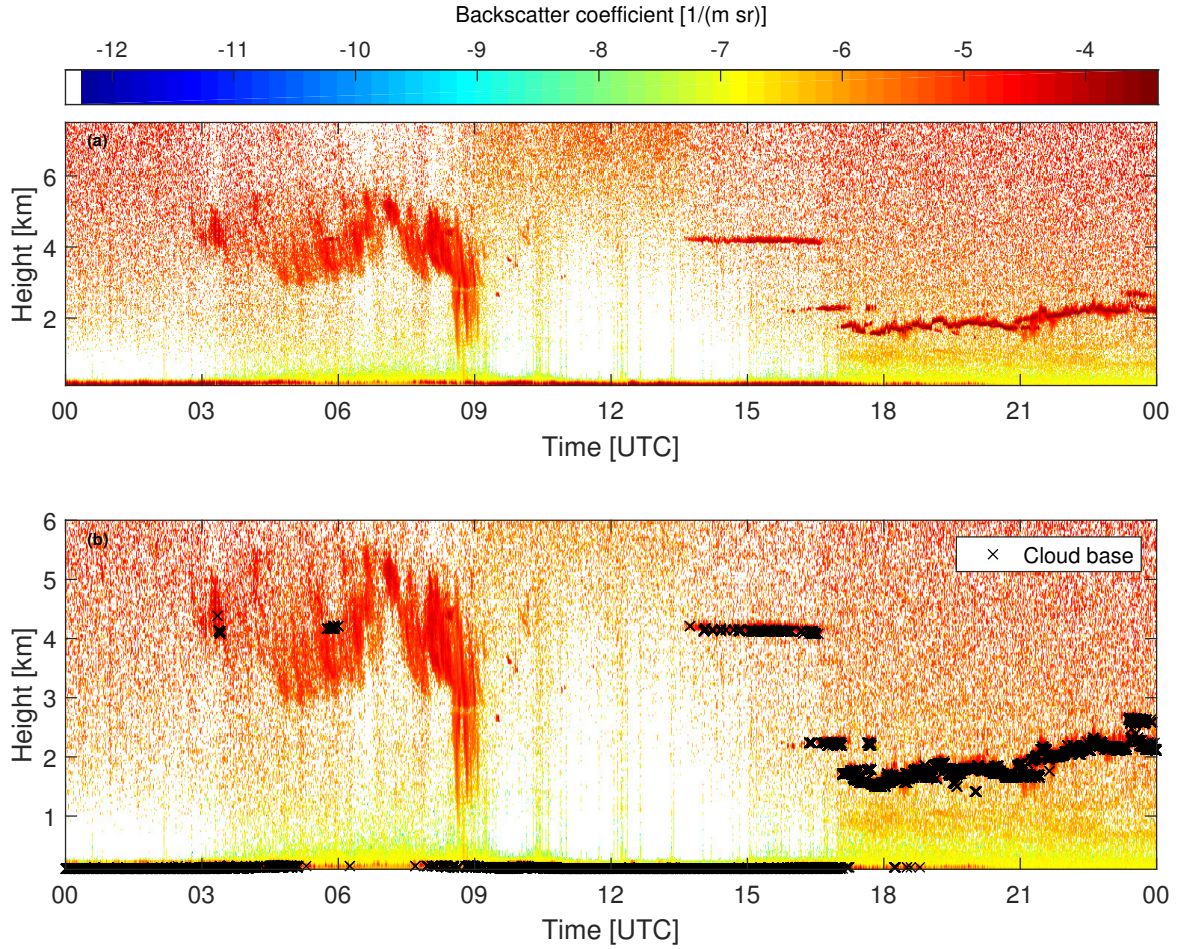
Figure 3.5: Backscatter coefficient from ceilometer after the interpolation to the reference instrument KAZR. The lower panel shows in addition the cloud base which is the first value where the backscatter coefficient is above $10^{-4}\,\mathrm{m}^{-1}\,\mathrm{sr}^{-1}$.

2.6 km height and another one at approximately 4.1 km height. After the height of the cloud base was derived from the attenuated backscatter coefficient, the corresponding interpolated cloud base temperature T_{cb} were obtained from the GDAS1 dataset.

Following the determining of H_{cb} and T_{cb} the height (H_{ct}) and the temperature (T_{ct}) of the cloud top were identified.

For this it is first settled whether a cloud exists or not. Using the reflectivity detected by KAZR it can be determined whether these values are finite or infinite. Therefore, at the existence of a cloud the corresponding signal is equal to one (i.e., signal is finite). If no cloud is detected the related signal is equal to zero (i.e., the signal is infinite). From this array of zeroes and ones, cloud bases are characterized by a switch from 0 to 1 whereas a cloud top is characterized by a switch from 1 to 0. Hereby it should be noted that cloud bases found in the KAZR data also contain the bases of virgae. This is the reason why CEIL data was used to derive the actual base of liquid layers.

Finally, it is checked whether the distance between cloud top and the adjacent cloud base is smaller than 1 km. If this is the case, the height of the cloud top is increased until no further cloud base is observed at a distance of below 1 km above cloud top.

Figure 3.6 a) illustrates the cloud tops as red circles as well as the reflectivity up to the height of 7.5 km. Data above this altitude, can not be compared with the ceilometer that is limited to 7.5 km height. Accordingly, no statement about the cloud top of the cloud between 1:30 UTC and 9 UTC can be made but it would not matter anyway since no liquid cloud base is observed by the CEIL (compare Figure 3.6). Moreover, it should be noted that the cloud tops for the values occurring in the boundary layer can be detected as well.

In the lower panel (Figure 3.6 b) the cloud bases are additionally marked as black X in the time-height cross-section of the reflectivity. For the calculation of the IWC it is important that a profile contains a pair of cloud tops and bases. Around 16 UTC the case occurs that a cloud base is detected in the two lower cloud layers, whereas no cloud base is indicated for 4.1 km height. Apparently, the ceilometer signal is attenuated too much in the lower cloud layers. Due to this attenuation the attenuated backscatter coefficient produced by the upper cloud layer is lower than the applied cloud-base detection threshold.

Before the ice water content of the crystals formed heterogeneously within the detected supercooled, liquid cloud layers can be derived, the reflectivity and temperature just below liquid cloud base must be determined. This is done in a similar way as described by *Bühl et al.* [2016], who derived the respective reflectivity and temperature values 60 m below cloud base. In his work, it is stated that no major changes of the particles micro-physical properties should occur, when values are obtained just 60 m below the liquid cloud base height. Nevertheless, 60 m distance is sufficient to minimize possible effects of cloud droplets on the radar reflectivity which is required for the calculation of the ice water content.

To obtain the required data 60 m below cloud base, the algorithm scans each profile and checks whether a cloud base and cloud top exists in a profile. For the cases where cloud top and base exists at the same time, the altitudes (H_{cb60}), temperature, and reflectivity are stored for the cloud top, cloud base and 60 m below the cloud base.

3.2.2   Data filtering

Once the parameters for cloud top, cloud base and for 60 m below cloud base were obtained the dataset is filtered in order to find the mixed phase cloud profiles, that comply to certain selection criteria. Herby, the LWP, the backscatter coefficient, the temperature and the geometrical thickness are taken into account for determining valid profiles. After application of all filter settings listed in Table 3.1, the amount of valid pairs of cloud top and cloud base reduce to the one shown in Figure 3.7. For all other cloud profiles shown in Figure 3.6 at least one of the selection criteria was not met.

For instance, all cloud layers observed below approximately 2.5 km height occurred at $T_{ct} > 0\,°C$ and thus are unlikely to contain ice crystals. The deep cirrus cloud observed before 9 UTC was not found to contain cloud droplets according to the CEIL observations of attenuated backscatter coefficient and thus valid cloud bases are missing for this layer. The
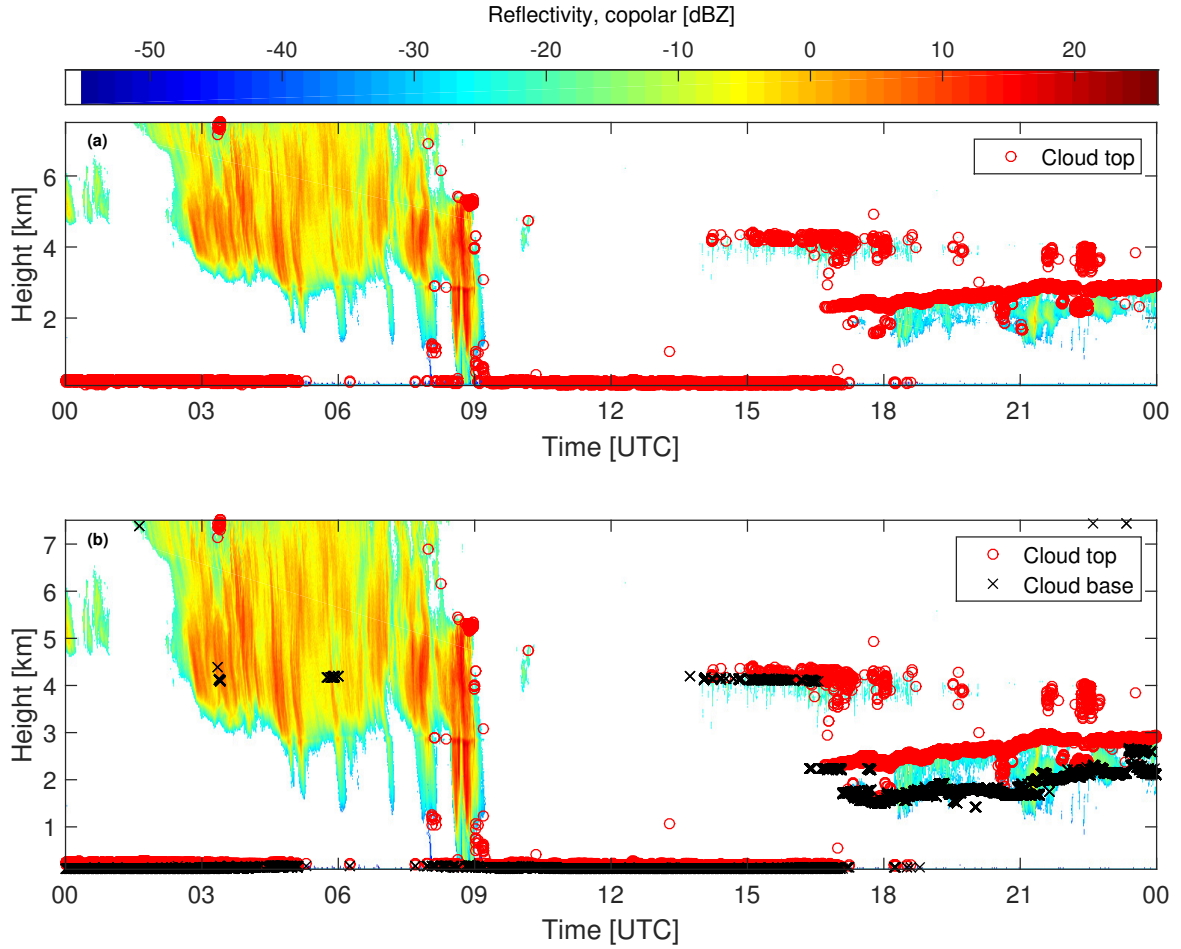
Figure 3.6: Reflectivity from the reference instrument KAZR with the cut height up to 7.5 km. Note that the reflectivity is cleaned with the algorithm from *Ewald et al.* [2015]. In (a) only the cloud top is presented. (b) shows cloud top and base as well.

only remaining valid cloud profiles were determined in the lofted cloud layer that occurred at 4 - 4.5 km height from 14 UTC to 17 UTC. As can be seen in the KAZR measurement of reflectivity, this supercooled liquid layer also produced some ice virgae. The liquid water path is a measure of the weight of liquid water droplets in the atmosphere per unit area. It indicates the total amount of water in the atmosphere. With low liquid water amounts follows a great uncertainty on the liquid water identification. *Shupe* [2007] states, that the liquid water path (LWP) has an uncertainty of $\sim 25 \, \mathrm{g \, m^{-2}}$. Within this work a lower LWP threshold of $10 \, \mathrm{g \, m^{-2}}$ was used to remove noise-induced false positive LWP values from the dataset.

In the scope of this study, only profiles that show a LWP between $10 \, \mathrm{g \, m^{-2}}$ and $500 \, \mathrm{g \, m^{-2}}$ were taken into account. Thus profiles showing lower LWP values are expected to contain ice only. In case of LWP values above $500 \, \mathrm{g \, m^{-2}}$ Mie scattering by large droplets affects the measurement in the profile. This happens for example, when large particles such as rain

Value	Threshold
LWP	$10\,\mathrm{g\,m^{-1}} \leq \mathrm{LWP} \leq 500\,\mathrm{g\,m^{-2}}$
Attenuated backscatter	$0\,\mathrm{m^{-1}\,sr^{-1}} \leq \mathrm{bscatt}_{NSA} \leq 10^{-4}\,\mathrm{m^{-1}\,sr^{-1}}$
	$0\,\mathrm{m^{-1}\,sr^{-1}} \leq \mathrm{bscatt}_{SGP} \leq 2{\cdot}10^{-5}\,\mathrm{m^{-1}\,sr^{-1}}$
Temperature	$-40\,^{\circ}\mathrm{C} \leq \mathrm{T}_{ct} \leq 0\,^{\circ}\mathrm{C}$
	$\mathrm{T}_{cb60} \leq 0\,^{\circ}\mathrm{C}$
Geometrical thickness	$300\,\mathrm{m}$

Table 3.1: Thresholds which were used to find valid values and the ice water content of a cloud.

droplets occur. Even though the rain might not reach the ground anyway, such large values for the liquid water path appear. From Figure 3.3c it can be seen that LWP values were mostly in the valid range required for this study. Only in the early morning of 6 August, LWP was occasionally below $10\,\mathrm{g\,m^{-2}}$.
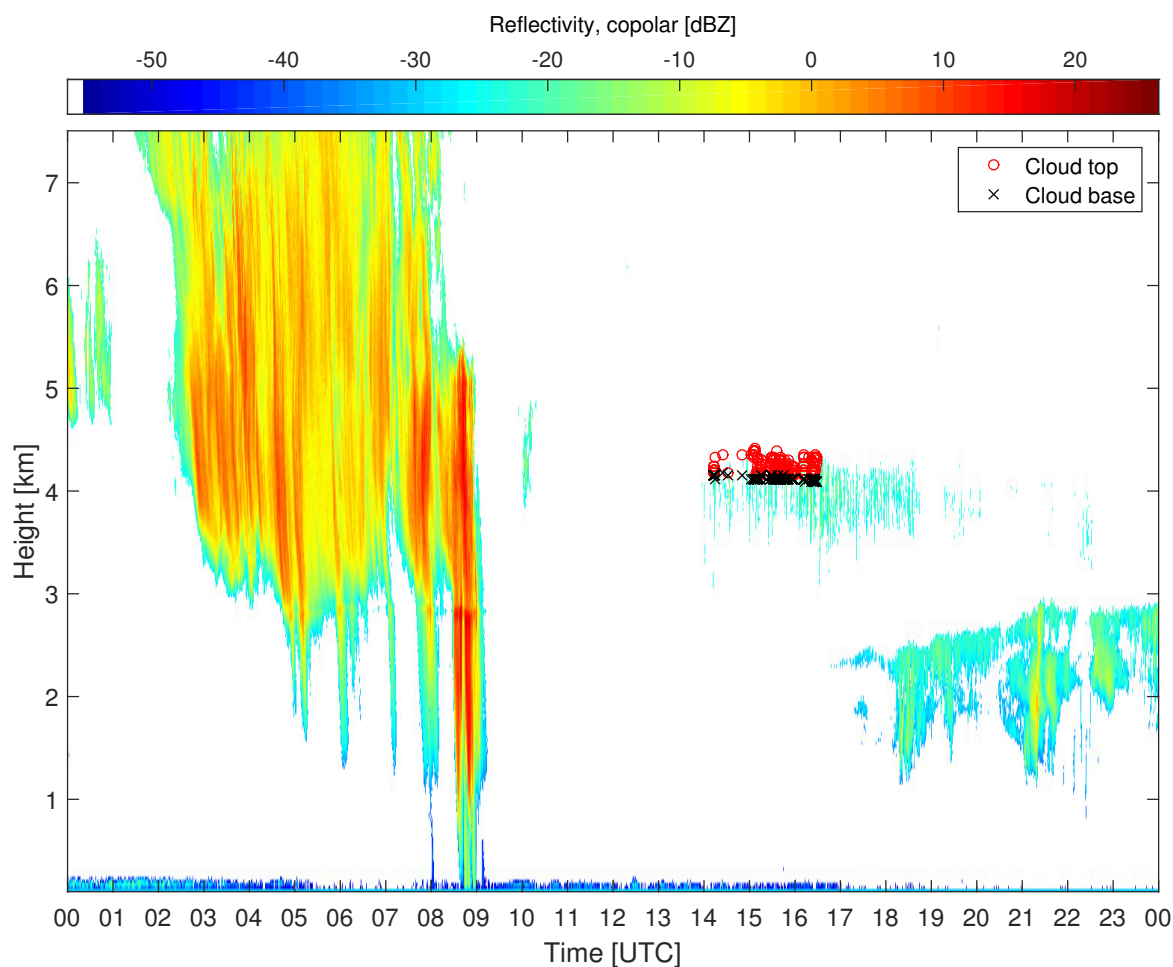
Figure 3.7: Reflectivity with the detected cloud bases and cloud tops after the filter was applied.

3.2.3   Calculation of the Ice Water Content

In the following section it will be described how the IWC at H_{cb60} is calculated for all profiles of pairs of cloud base and cloud top that met the filter requirements listed in Table 3.1.
Hogan et al. [2006] showed that there is a relationship between the temperature, the radar reflectivity and the IWC. Due to additional corrections, such as for small particles and some calculations by using the particle diameter, mass, and area the particle size can be neglected while calculating the IWC.

$$log_{10}(IWC) = (0.000242)ZT + 0.0699Z - 0.0186T - 1.63 \qquad (3.1)$$

The units of IWC, Z, and T are $g \, m^{-3}$, dBZ, and °C, respectively. The relations presented here are for a $35 \, GHz$ radar.
In order to calculate the IWC with the formula 3.1 temperatures are converted from Kelvin to °C. In order to have a better comparison to *Bühl et al.* [2016], the ice water content is converted from $g \, m^{-3}$ to $kg \, m^{-3}$.
After the definition of the IWC the mean, median and standard deviation of the IWC were calculated in $5 \, °C$ cloud top temperature intervals.
In the next Chapter the relationship between the calculated IWC_{cb60} and the cloud top temperature T_{ct} will be presented and discussed afterwards.

Chapter 4

Results

In this chapter the results of the statistical analysis of the calculated IWC from cloud base properties in relation to the cloud top temperature is presented. At cloud top, the temperature is lowest and thus ice formation efficiency reaches its maximum. Therefore, T_{ct} is used as the reference value for the evaluation of the ice water content formed in a supercooled liquid cloud layer.

1 day of NSA and 20 days of SGP MWR data is not available (see Appendix 6) and is therefore missing in the statistical analyses. Therefore, these days are missing in the statistical analyses of the ice water content.

First the statistics based on the combination of the ceilometer and radar are presented in Section 4.1. In Section 4.2 an evaluation of the IWC at NSA is performed by comparing the statistics from the CEIL-algorithm with the HSRL-algorithm.

In this study, records of NSA and SGP in 2014 were investigated. The following figures show the NSA dataset in blue and the one from SGP in red.

4.1   Statistics with CEIL

The purpose of this work is to characterize if there is a latitudinal dependence of the IWC formed in shallow supercooled liquid clouds. For this purpose, a cloud profile comparison between the two stations at NSA and SGP was performed and results are presented in this chapter.

Profiles of mixed-phase clouds were determined due to a filter explained in Section 3.2.2. The number of profiles derived within intervals of $5\,\mathrm{K}$ between $-40\,^{\circ}\mathrm{C}$ and $0\,^{\circ}\mathrm{C}$ are shown in Figure 4.1. There is a significant difference in the observed cases between NSA and SGP, where NSA has $411.1 \cdot 10^3$ and SGP $19.3 \cdot 10^3$, this is an order of magnitude lower than at NSA and it is only $4.5\,\%$ of the total observed cloud profiles at NSA and SGP. The most cloud profiles at NSA were detected at $-12.5\,^{\circ}\mathrm{C}$ which are $30\,\%$ of the total detected mixed-phase cloud of NSA. The most observed profiles for SGP are observed between $-5\,^{\circ}\mathrm{C}$ and $0\,^{\circ}\mathrm{C}$ with an amount of 33.2% (see Table 6.2 in the Appendix for further details). Figure
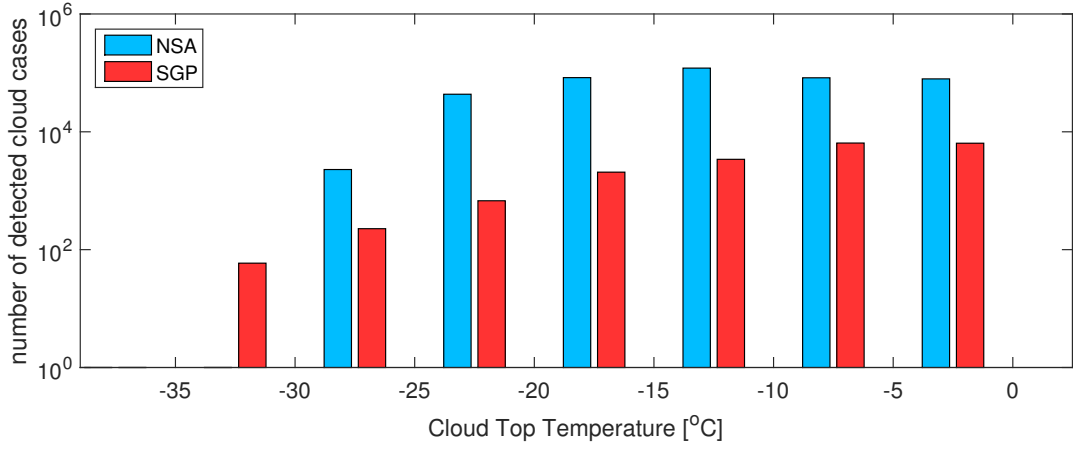
Figure 4.1: Comparison of the cloud cases from the two stations NSA (blue) and SGP (red) in 2014. On the x-axis the number of cases involved are shown for each 5 K interval of cloud top temperature.

4.1 shows how the number of observed cloud cases decrease as the temperature decreases at SGP, whereas the maximum of observed cloud profiles at NSA is at - 15 °C to - 10 °C. To further quantify the process of ice formation, the IWC related to the cloud top temperature was computed for the cloud profiles which were detected with the algorithm. The average and median IWC for all cloud profiles are shown as well in Figure 4.2, where dashed and solid lines indicate the mean and the median values, respectively. For both stations it is visible, that the IWC generally increased with decreasing cloud top temperature. The sub-tropics have larger IWCs than those in the Arctic region for the same cloud top temperature except for the 5 K intervals around - 32.5 °C, - 12.5 °C and - 2.5 °C, for which the median values are larger at NSA than at SGP.

Furthermore, the cloud top temperatures range between - 29.3 °C and - 0.2 °C at NSA, and between - 34.1 °C and - 0.8 °C at SGP. This shows that the lowest recorded temperature of a supercooled liquid layer at SGP is approximately 5 K lower than the respective lowest recorded temperature at NSA. This can also be seen in Figure 4.1 where it is shown that no more cloud profiles are detected below - 30 °C at NSA.

In Figure 4.2 the mean IWC in general is higher than the median IWC, thus the distribution of data points shows a negative skewness. That follows, that the measured IWC values are not Gaussian distributed and has therefore an asymmetric probability distribution. When the median is lower than the mean, the distribution is skewed to lower IWC values and vice versa. At both stations the maximum difference between mean and median IWC is observed at - 12.5 °C, where the associated IWC differences at NSA are $1.64 \cdot 10^{-5} \, \mathrm{kg \, m^{-3}}$ and at SGP $1.95 \cdot 10^{-5} \, \mathrm{kg \, m^{-3}}$. A minimum difference between mean and median is monitored in the 5 K interval around - 22.5 °C and - 2.5 °C in NSA and SGP, respectively. Also at around - 12.5 °C the maximum standard deviation is observed at both stations. A more detailed statistical overview is presented in Table 6.2 in the Appendix 6.
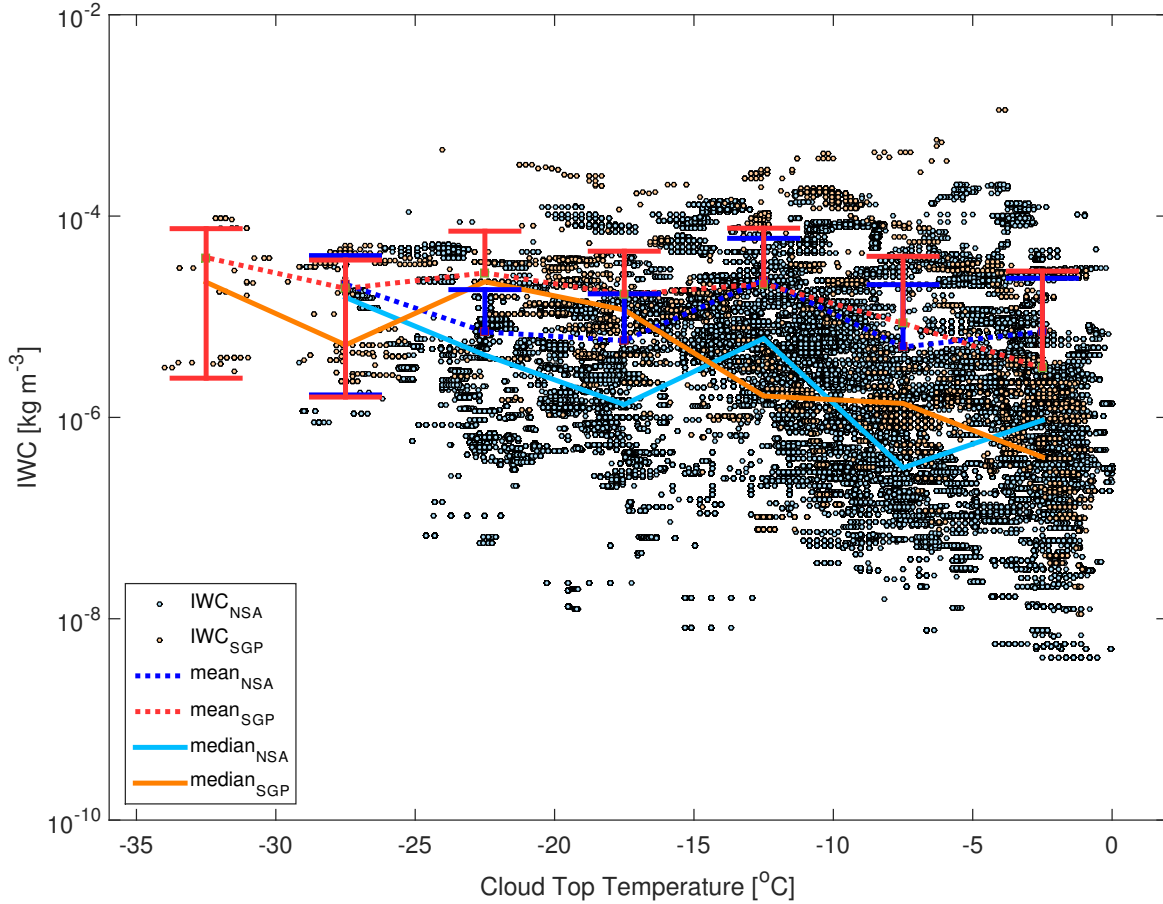
Figure 4.2: Values of IWC (dots) obtained 60 m below the base of liquid layers by using the
Z-T-IWC equation from *Hogan et al.* [2006]. The mean (dashed line) and median (solid line) IWC
calculated in 5 K intervals is shown as well in the respective colour for the station. Error bars
denote the standard deviation. The IWC on the y-axis is scaled logarithmic and the x-axis shows
the corresponding cloud top temperatures. Lower branches of error bars are partly missing when
high standard deviations would lead to negative values which cannot be presented in logarithmic
scale.

4.2   NSA Statistic with HSRL

For inter-comparison, the IWC statistics based on a methodology where the ceilometer data
was replaced by HSRL data is presented in this section. The advantage the HSRL holds
over the ceilometer is that it provides the actual particle backscatter coefficient, that is not
affected by attenuation of aerosols and cloud particles. Furthermore, the cloud detection
height is not limited to 7.5 km altitude.

First of all, it is obvious from Figure 4.3, that the HSRL detected more cloud cases
$(642.2 \cdot 10^3)$ compared to the use of CEIL. According to this the amount of maximum de-
tected cloud profiles, with HSRL, is shifted to the temperature interval around - 7.5 °C and
takes 25.0 % of the total detected mixed-phase cloud profiles at NSA.
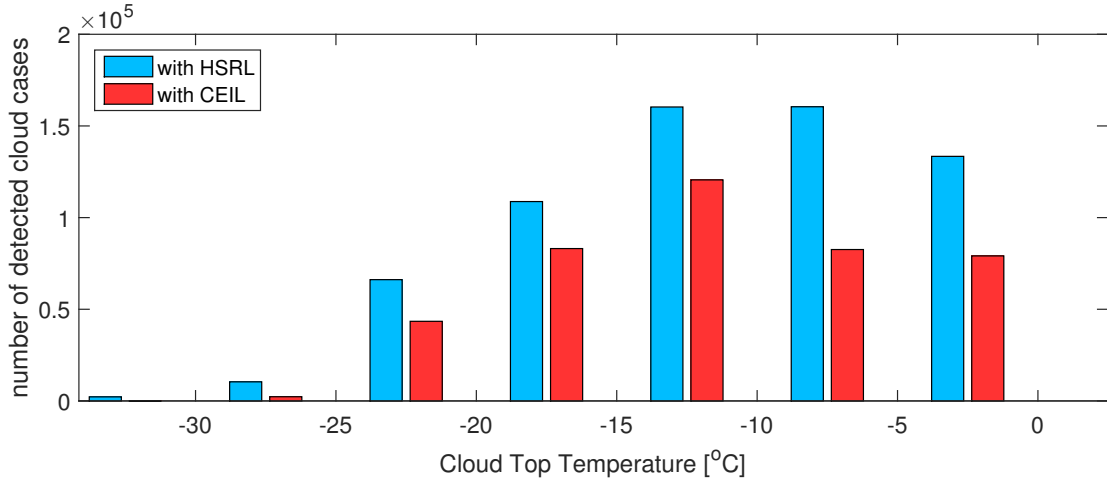
Figure 4.3: Histogram for NSA by using the HSRL (blue) as cloud base determination instrument and in red the cloud profiles determined by CEIL. On the x-axis the number of cloud profiles involved are shown for each $5\,\mathrm{K}$ interval of cloud top temperature.

By comparing the statistics of CEIL (Figure 4.1) and HSRL (Figure 4.3) it can be seen, that the range of absolute IWC varies between the same values as were detected with the CEIL algorithm, namely $4.07 \cdot 10^{-9}\,\mathrm{kg\,m^{-3}}$ and $2.09 \cdot 10^{-4}\,\mathrm{kg\,m^{-3}}$. Since the HSRL has a larger detection range, it is possible that it can identify liquid water layers at lower temperatures, as well. Therefore, the absolute temperature range is between $-40.0\,^{\circ}\mathrm{C}$ and $0\,^{\circ}\mathrm{C}$. Comparing Figure 4.2 and Figure 4.4 it is visible that the HSRL can detect liquid cloud layers at a lower temperature than CEIL.

The mean values acquired from using CEIL and HSRL are similar, and show no significant difference. Both have the minimum IWC in the interval around $-7.5\,^{\circ}\mathrm{C}$ and the maximum IWC at $-12.5\,^{\circ}\mathrm{C}$. Note, that the associated IWC extreme values are $3.00 \cdot 10^{-6}\,\mathrm{kg\,m^{-3}}$ and $2.12 \cdot 10^{-5}\,\mathrm{kg\,m^{-3}}$, whereas the values for the IWC observed by CEIL are $4.97 \cdot 10^{-6}\,\mathrm{kg\,m^{-3}}$ and $2.24 \cdot 10^{-5}\,\mathrm{kg\,m^{-3}}$.

The maximum median calculated with the HSRL data is approximately one order of magnitude higher than the one obtained with CEIL.

Over the entire cloud temperature range the mean lays above the median, and therefore a negative skewness exists here as well. A more detailed statistical comparison of CEIL and HSRL can be found in Table 6.4 in Appendix 6.
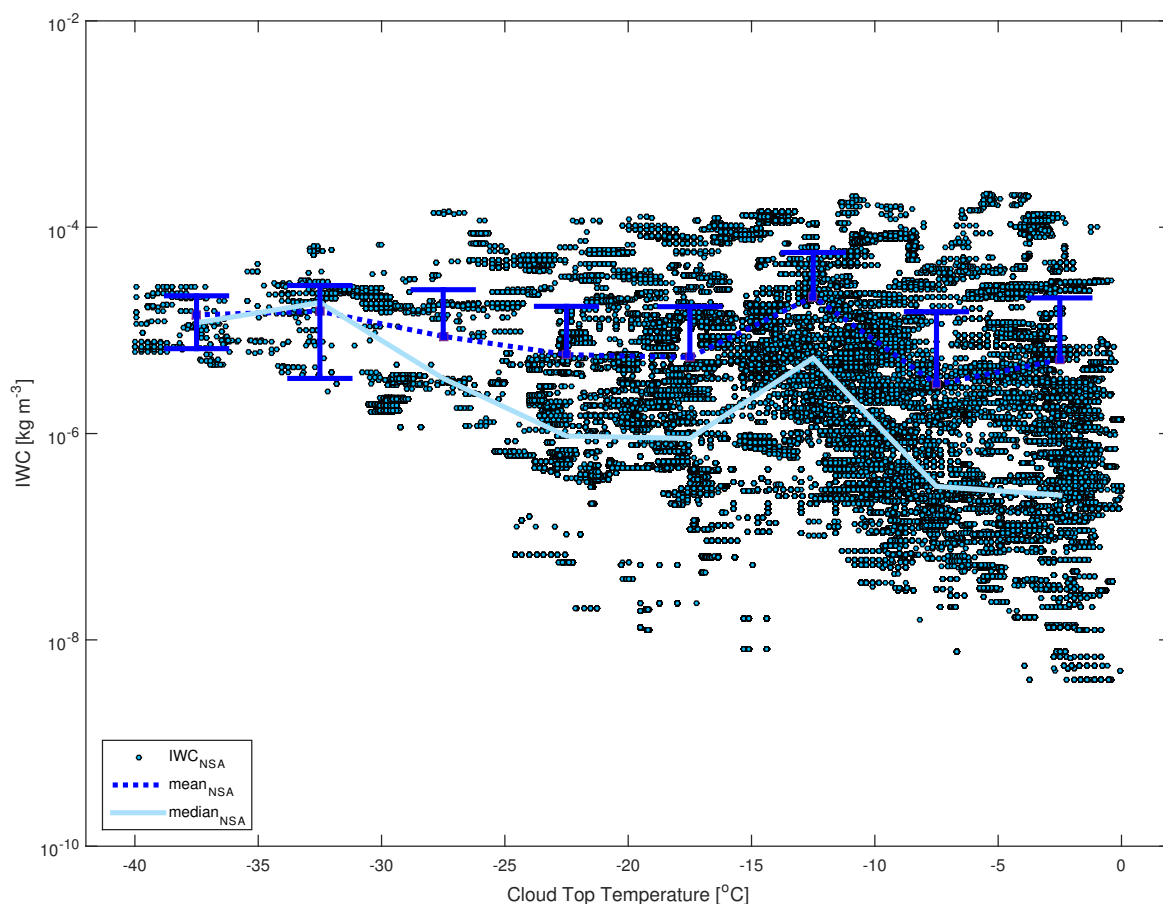
Figure 4.4: Values of IWC (dots) obtained 60 m below the base of liquid layers by using the Z-T-IWC equation from *Hogan et al.* [2006]. The mean (dashed line), median (light blue, solid line) IWC calculated in 5 K intervals is shown for the HSRL. Error bars denote the standard deviation. The IWC on the y-axis is scaled logarithmic and the x-axis shows the corresponding cloud top temperature. Lower branches of error bars are partly missing when high standard deviations would lead to negative values which cannot be presented in logarithmic scale.

Chapter 5

Discussion

On the basis of the methodology (Chapter 3) it should be evaluated within this work if there is a latitudinal variability of the ice water content in shallow, mixed-phase clouds, or if statistical effects, such as ones introduced by the instrumentation hamper a comparison of two different stations that are equipped with mostly the same instruments.

The analysis of the data revealed a similarity to the studies of *Bühl et al.* [2016] and *Zhang et al.* [2010]. The best agreement of the IWC distribution can be found between the NSA dataset and *Bühl et al.* [2016]. Furthermore, the comparison with CEIL and HSRL at NSA shows similar results of the IWC.

One important question is if regional differences also affect the relation between cloud top temperature and IWC 60 m below cloud base, produced within mixed-phase cloud layers.

5.1 Statistics with CEIL

The analysis of the data shows distinct differences between the observed cloud profiles at NSA and SGP. More mixed-phase cloud profiles were found at NSA than at SGP. It should be noted that for 2014 MWR data was missing for 1 day at NSA and 20 days at SGP. This could lead to a slightly lower number of observed profiles at SGP, but cannot explain the observed differences. Another instrumental effect on the data set could be the maximum detection height of 7.5 km of the ceilometer. According to the latitude-dependent standard atmospheres [*Cole and Kantor* [1978]], temperatures above -40 °C can well appear in the subtropics at heights above 7.5 km, whereas it is unlikely for the Arctic region. At NSA, it was also found that the datasets obtained based on CEIL and HSRL agree rather well, making an effect of the reduced detection height of CEIL unlikely in the Arctic. Nevertheless, due to the limitation of the CEIL, this study cannot draw a conclusion about whether the increasing ratio of NSA to SGP cases with decreasing temperature, shown in Figure 4.1 is due to meteorological or instrumental effects. Data from micropulse lidar (MPL) which is also available at both sites and provides data up to 15 km height, could be an alternative to the CEIL. Unfortunately, the MPL data is not calibrated and therefore no attenuated backscatter coefficient is available from this instrument. The ARM archive

provides a cloud layer product based on a study of *Wang and Sassen* [2001]. This algorithm however does not distinguish between the base of virgae and of liquid layers and is thus not suitable for this study that requires the base of the liquid cloud layers.

The IWC is expected to increase with decreasing cloud top temperatures, previous studies such as *Zhang et al.* [2010] and *Bühl et al.* [2016] showed an increase of IWC with decreasing temperature, as well. It can be seen in Figure 4.2, for NSA the IWC is slightly increasing up to -12.5 °C and then after reaching the peak it decreases slightly with decreasing temperature but it is still higher than at 0 °C. In this study a peak in IWC was observed in the cloud top temperature interval between -10 °C and -15 °C at NSA. The peak at -12.5 °C is due to the use of 5 K temperature intervals of the cloud top instead of 2.5 K intervals, which would give a peak at -15 °C (not shown). It is remarkable, that this study can not observe an obvious peak between temperatures at -10 °C and -15 °C at SGP, this can lead to the conclusion that there is a latitude dependence on the IWC. Both *Zhang et al.* [2010] and *Bühl et al.* [2016] observe an IWC peak around -15 °C as well. According to *Bühl et al.* [2016], the peak in IWC at around -15 °C is also caused by the large scattering area of the horizontally aligned dendritic ice crystals that are usually formed at -15 °C. Therefore, the missing peak in IWC in this temperature interval at SGP could hypothetically be caused by the production of much more but much smaller ice crystals (with lower axis ratios) at this site compared to other sites. Liquid cloud layers with the lowest cloud tops for which IWC was detected could be found at SGP. Since there is no obvious peak observed in the sub-tropics it can also be assumed that this is due to the different aerosol regimes in the certain area. *Michalsky et al.* [2010] and *Yin and Min* [2014] reported an average aerosol optical depth of 0.15 and 0.05 for SGP and NSA, respectively. It should be noted, that the actual vertical aerosol profiling for NSA and SGP was not investigated in this study.

Zhang et al. [2010] used CALIPSO and CloudSat measurements to study the latitudinal difference of mid-level clouds warmer than -40 °C. It was found that mixed-phase clouds persist at temperatures as low as -30 °C, especially in the tropics. The investigation presented here shows a cloud top temperature range for SGP below -30 °C. At NSA the observed cloud top temperatures were never below -25 °C.

A fluctuation of the median IWC can be observed at both stations. The IWC at SGP is in general higher than the IWC at NSA. For different cloud top temperatures (-2.5 °C, -12.5 °C and -27.5 °C) the median IWC at NSA is higher than at SGP.

Some of the findings, such as a regional variability and that ice is formed in shallow mixed-phase clouds for Leipzig, are already observed in previous studies from *Zhang et al.* [2010] and *Bühl et al.* [2016], respectively. A seasonal and regional difference in properties of mid-level, mix-phase clouds could be found from the outcomes of *Zhang et al.* [2010], but since a satellite based retrieval was used it cannot be directly compared with ground-based remote sensing instruments, because the detection thresholds of the space-borne instruments are much higher. Therefore, a sufficient statement about regional variability of the IWC cannot be made from this study.

The study from *Bühl et al.* [2016] combined measurements of cloud radar and lidar and a retrieval were quantified, but a comparison with other stations than Leipzig was not done. *Bühl et al.* [2016] also used an algorithm that identifies coherent cloud layers instead of single profiles. This could lead to a potential mismatch in the IWC-to-temperature relationship between the Leipzig dataset and the ones shown in this study.

The reason of less detected shallow mixed-phase cloud profiles at SGP could be due to the small detection range up to 7.5 km. Therefore, it is hard to generalize and compare the stations at NSA and SGP since some of the mixed-phase cloud profiles are above this range. However, other instrumental issues could also be a reason for the misdetection of cloud profiles. There are uncertainties in the radar calibration that were not included yet. In addition, no comparison of the calibration of the radar at NSA and SGP were made. Furthermore, the attenuation of atmospheric gases and liquid water such as rain is not implemented in the algorithm which can lead to exclude some of the first detected cloud profiles.

5.2 Statistics with HSRL in NSA

An alternative to indicate shallow, mixed-phase clouds is the combination of CEIL and KAZR, since the detection height of CEIL is relative small compared to the other instruments that were used in this study. It was expected that with the algorithm presented here some of the clouds above 7.5 km were neglected and an additional static with HSRL was done.

Large differences were observed already in the amount of detected cloud profiles. HSRL has approximately $200 \cdot 10^3$ more cloud profiles as there were detected with CEIL. This is due to the fact that the detection range of CEIL is small compared to HSRL, but it can also be the advantages of HSRL such as the direct calculation of the particle backscatter coefficient. The CEIL is independent of the transmission and measures the attenuated backscatter only, whereas the HSRL backscatter is integrated over the column of air.

In Figure 4.4 an IWC peak between cloud top temperatures at - 10 °C and - 15 °C can be observed, the median is also smooth compared to the observations with CEIL. The more stable median could be a reason of the limited detection height of CEIL. The ceilometer laser pulse is attenuated when it hits clouds whereas the HSRL measures the backscatter coefficient directly. The advantage of the HSRL could lead to better results and therefore a more stable median is observed. More reliable datasets can be observed with HSRL due to its larger detection range. Since only SGP and NSA are compared, it is difficult to conclude if the use of CEIL yields a misdetection of cloud bases or not. Maybe an additional station shows different results for the IWC while using the HSRL instead of CEIL.

Chapter 6

Summary and Conclusion

To understand the role of clouds in the atmosphere-earth climate system, it is necessary to characterize micro- and macro-physical properties of clouds. In this study a long-term observation of the IWC at the ARM sites NSA and SGP were presented for 2014. The combination of radar, lidar, microwave radiometer and modelled temperature profiles was used as the basis for the algorithm developed and presented in this work.

Firstly, cloud tops and bases of supercooled liquid cloud layers needed to be defined. Secondly, related parameters such as temperature and reflectivity were determined. With the algorithm described in Section 3.2 and the filtering of the data the IWC of mixed-phase clouds 60 m below the cloud base was calculated.

Wang and Sassen [2001] presented that the different lidar and radar wavelengths complement each other and will therefore result in a better cloud detection.

Thresholds from previous studies such as from Cloudnet [*Illingworth et al.* [2007]], the lidar / radar combination from *Bühl et al.* [2013], [2016], and from *Zhang et al.* [2010] were used to characterize heterogeneous ice formation.

This study presents an algorithm that defines shallow, mixed-phase clouds with cloud top temperatures warmer than - 40 °C. The IWC formed by supercooled clouds of a certain cloud top temperature was obtained at a height of 60 m below their liquid base to be free of droplet artefacts. To minimize effects of secondary ice formation and ice multiplication, the maximum depth of the liquid layers was limited to 300 m. In general, IWC increased with decreasing temperature at both sites. A local peak of IWC was found to be between cloud top temperatures of - 10 °C and - 15 °C at NSA. A corresponding peak was not found at SGP, which is inconsistent to the results of *Bühl et al.* [2016] and *Zhang et al.* [2010]. At SGP, the shallow, mixed-phase clouds persisted at temperatures as low as - 30 °C. For the same cloud top temperature, the IWC of sub-tropic (SGP) clouds were larger than Arctic (NSA) clouds. More cloud profiles were determined at NSA than SGP, which leads to the assumption that the maximum detection height of CEIL was to low to detected all cloud layers in the cloud-top-temperature range between - 40 °C and 0 °C.

The comparison between CEIL and HSRL data, which was only possible for NSA, showed a difference in the amount of detected cloud profiles. A peak in the temperature interval

between -10 °C to -15 °C was also remarkable in the HSRL retrieval.

The algorithm developed to classify shallow, mixed-phase clouds is used for the ARM sites. Further studies should be done to investigate the IWC on clouds at other latitudes as well, especially in the southern hemisphere, to get a global comparison of the IWC. Moreover, the instrumentation should be the same for all stations. From the comparison of CEIL and HSRL it was shown that some of the mixed-phase clouds will be lost due to the limited detection height of 7.5 km. The radars at NSA and SGP were in addition not proofed for the calibration which can lead to errors in the statistical analysis. The algorithm and instrument combination still needs an improvement. An investigation of the attenuation of the radar signal by atmospheric gases or liquid water could be an improvement of the algorithm. In addition, a valid comparison with satellites and ground-based measurements needs to be done to get a better understanding of the ice nucleation in mixed-phase clouds.

Overall, more measurements over longer time periods at different latitudes would improve the investigation of the regional variability of the ice water content in supercooled stratiform clouds.

Bibliography

Ansmann, A., M. Tesche, P. Seifert, D. Althausen, R. Engelmann, J. Fruntke, U. Wandinger, I. Mattis, and D. Mller (2009), Evolution of the ice phase in tropical altocumulus: Samum lidar observations over Cape Verde, *Journal of Geophysical Research, 114*(D17), doi: 10.1029/2008jd011659.

ARM (2015a), Atmospheric radiation measurement (arm) research facility, `https://www.arm.gov`.

ARM (2015b), North slope of alaska main site barrow, `https://www.flickr.com/photos/armgov/21947273796/in/album-72157623930532565/`.

ARM (2015c), Central facility at southern great plains site, `https://www.flickr.com/photos/armgov/4857656636/in/album-72157623930532361/`.

Bühl, J., A. Ansmann, P. Seifert, H. Baars, and R. Engelmann (2013), Toward a quantitative characterization of heterogeneous ice formation with lidar/radar: Comparison of calipso/cloudsat with ground-based observations, *Geophysical Research Letters, 40*(16), 4404-4408, doi: 10.1002/grl.50792.

Bühl, J., A. Myagkov, P. Seifert, and A. Ansmann (2016), Relation between ice and liquid water mass in mixed-phase cloud layers measured with cloudnet, *Submitted to Atmospheric Chemistry and Physics (Discussions)*.

Cole, A. E., and A. J. Kantor (1978), Air force reference atmosphere, *Air Force Geophysics Lab Hanscom AFB MA TR-78-0051*, aDA058505.

Ewald, F., C. Winkler, and T. Zinner (2015), Reconstruction of cloud geometry using a scanning cloud radar, *Atmospheric Measurement Techniques, 8*(6), 2491-2508, doi: 10.5194/amt-8-2491-2015.

Hogan, R. J., M. P. Mittermaier, and A. J. Illingworth (2006), The retrieval of ice water content from radar reflectivity factor and temperature and its use in evaluating a mesoscale model, *Journal of Applied Meteorology and Climatology, 45*(2), 301-317, doi: 10.1175/jam2340.1.

Hoose, C., and O. Möhler (2012), Heterogeneous ice nucleation on atmospheric aerosols: a review of results from laboratory experiments, *Atmospheric Chemistry and Physics*, *12*(20), 9817-9854, doi: 10.5194/acp-12-9817-2012.

Icestories (2015), Barrow, alaska on the polar region map, `http://icestories.exploratorium.edu/dispatches/wp-content/uploads/assets/maps`.

Illingworth, A. J., R. J. Hogan, E. J. OâConnor, D. Bouniol, J. Delano, J. Pelon, A. Protat, M. E. Brooks, N. Gaussiat, D. R. Wilson, and et al. (2007), Cloudnet, *Bulletin of the American Meteorological Society*, *88*(6), 883-898, doi: 10.1175/bams-88-6-883.

Kanitz, T., P. Seifert, A. Ansmann, R. Engelmann, D. Althausen, C. Casiccia, and E. G. Rohwer (2011), Contrasting the impact of aerosols at northern and southern midlatitudes on heterogeneous ice formation, *Geophysical Research Letters*, *38*(17), doi: 10.1029/2011gl048532.

Korolev, A., and P. R. Field (2008), The effect of dynamics on mixed-phase clouds: Theoretical considerations, *Journal of the Atmospheric Sciences*, *65*(1), 66-86, doi: 10.1175/2007jas2355.1.

Korolev, A. V., G. A. Isaac, S. G. Cober, J. W. Strapp, and J. Hallett (2003), Microphysical characterization of mixed-phase clouds, *Q. J. R. Meteorol. Soc.*, *129*(587), 39-65, doi: 10.1256/qj.01.204.

Liljegren, J. C., E. E. Clothiaux, G. G. Mace, S. Kato, and X. Dong (2001), A new retrieval for cloud liquid water path using a ground-based microwave radiometer and measurements of cloud temperature, *Journal of Geophysical Research*, *106*(D13), 14485, doi: 10.1029/2000jd900817.

Michalsky, J., F. Denn, C. Flynn, G. Hodges, P. Kiedron, A. Koontz, J. Schlemmer, and S. E. Schwartz (2010), Climatology of aerosol optical depth in north-central oklahoma: 1992â2008, *Journal of Geophysical Research*, *115*(D7), doi: 10.1029/2009jd012197.

Morris, V. (2006), Microwave radiometer handbook.

Mülmenstädt, J., O. Sourdeval, J. Delanoë, and J. Quaas (2015), Frequency of occurrence of rain from liquid-, mixed-, and ice-phase clouds derived from a-train satellite retrievals, *Geophysical Research Letters*, *42*(15), 6502â6509, doi: 10.1002/2015gl064604.

Nakamura, N., and A. H. Oort (1988), Atmospheric heat budgets of the polar regions, *Journal of Geophysical Research*, *93*(D8), 95109524, doi: 10.1029/jd093id08p09510.

Oceanic, N., and A. Administration (2015), Global data assimilation system (gdas1) archive information, `http://ready.arl.noaa.gov/gdas1.php`.

Peters, G., and U. Görsdorf (2011), Wolkenradar - prinzipien und messungen, *promet*, *3/4*(36), 144-153.

Scarino, A. J., M. D. Obland, J. D. Fast, S. P. Burton, R. A. Ferrare, C. A. Hostetler, L. K. Berg, B. Lefer, C. Haman, J. W. Hair, and et al. (2014), Comparison of mixed layer heights from airborne high spectral resolution lidar, ground-based measurements, and the wrf-chem model during calnex and cares, *Atmospheric Chemistry and Physics*, *14*(11), 5547â5560, doi: 10.5194/acp-14-5547-2014.

Seifert, P., A. Ansmann, I. Mattis, U. Wandinger, M. Tesche, R. Engelmann, D. Mller, C. Prez, and K. Haustein (2010), Saharan dust and heterogeneous ice formation: Eleven years of cloud observations at a central European earlinet site, *Journal of Geophysical Research*, *115*(D20), doi: 10.1029/2009jd013222.

Seifert, P., A. Ansmann, S. Gro, V. Freudenthaler, B. Heinold, A. Hiebsch, I. Mattis, J. Schmidt, F. Schnell, M. Tesche, and et al. (2011), Ice formation in ash-influenced clouds after the eruption of the eyjafjallajkull volcano in April 2010, *Journal of Geophysical Research*, *116*, doi: 10.1029/2011jd015702.

Seifert, P., C. Kunz, H. Baars, A. Ansmann, J. Bhl, F. Senf, R. Engelmann, D. Althausen, and P. Artaxo (2015), Seasonal variability of heterogeneous ice formation in stratiform clouds over the amazon basin, *Geophysical Research Letters*, *42*(13), 5587-5593, doi: 10.1002/2015gl064068.

Shupe, M. D. (2007), A ground-based multisensor cloud phase classifier, *Geophysical Research Letters*, *34*(22), doi: 10.1029/2007gl031008.

Stamnes, K., R. G. Ellingson, J. A. Curry, J. E. Walsh, and B. D. Zak (1999), Review of science issues, deployment strategy, and status for the arm north slope of alaskaâadjacent arctic ocean climate research site, *Journal of Climate*, *12*(1), 46-63, doi: 10.1175/1520-0442-12.1.46.

Sun, Z., and K. P. Shine (1994), Studies of the radiative properties of ice and mixed-phase clouds, *Quarterly Journal of the Royal Meteorological Society*, *120*(515), 111-137, doi: 10.1002/qj.49712051508.

TROPOS (2015), Leibniz-institut für troposphärenforschung e.v., technology at tropos remote sensing, `http://www.tropos.de/en/research/projects-infrastructures-technology/technology-at-tropos/`.

Wang, Z., and K. Sassen (2001), Cloud type and macrophysical property retrieval using multiple remote sensors, *Journal of Applied Meteorology*, *40*(10), 1665-1682, doi: 10.1175/1520-0450(2001)040¡1665:ctampr¿2.0.co;2.

Widener, K., N. Bharadwaj, and K. Johnson (2012), Ka-band arm zenith radar (kazr) handbook.

Wikimedia (2015), Mercator-projection, `https://upload.wikimedia.org/wikipedia/commons/thumb/7/74/Mercator-projection.jpg/773px-Mercator-projection.jpg`.

Yin, B., and Q. Min (2014), Climatology of aerosol and cloud optical properties at the atmospheric radiation measurements climate research facility barrow and atqasuk sites, *Journal of Geophysical Research*, *119*(4), 1820-1834, doi: 10.1002/2013jd020296.

Zhang, D., Z. Wang, and D. Liu (2010), A global view of midlevel liquid-layer topped stratiform cloud distribution and phase partition from calipso and cloudsat measurements, *Journal of Geophysical Research*, *115*, doi: 10.1029/2009jd012143.

Zhang, D., Z. Wang, A. Heymsfield, J. Fan, D. Liu, and M. Zhao (2012), Quantifying the impact of dust on heterogeneous ice generation in midlevel supercooled stratiform clouds, *Geophysical Research Letters*, *39*(18), doi: 10.1029/2012gl052831.

Zhang, T., T. E. Osterkamp, and K. Stamnes (1997), Effects of climate on the active layer and permafrost on the north slope of alaska, u.s.a., *Permafrost and Periglacial Processes*, *8*(1), 45-67, doi: 10.1002/(sici)1099-1530(199701)8:1¡45::aid-ppp240¿3.0.co;2-k.

List of missing MWR data

North Slope of Alaska	01 October 2014
Southern Great Plains	12 January 2014
	08 February 2014
	09 February 2014
	16 February 2014
	17 February 2014
	23 February 2014
	14 June 2014
	15 June 2014
	26 June 2014
	13 July 2014
	02 August 2014
	03 August 2014
	17 August 2014
	07 September 2014
	27 September 2014
	28 September 2014
	18 October 2014
	19 October 2014
	26 October 2014
	02 November 2014

Statistic with CEIL

	cloud profiles [10^3]	Temperature [°C]	amount [%]
NSA			
total	411.1	–	95.5
min	3.1	- 27.5	0.75
max	124.4	- 12.5	30.3
SGP			
total	19.3	–	4.5
min	0.06	- 32.5	0.31
max	6.4	- 2.5	33.2

Table 6.1: Table of the cases, which were determined using the algorithm presented in Chapter 3. Presented are the total number of cases observed at each station (*total*), the temperature interval with the fewest cases (*min*) and with the maximum cases (*max*). The associated percentages are given with respect to the *total* amount of cloud profiles of the two stations NSA and SGP. For *min* and *max*, the percentage corresponding to the observed cloud cases from the respective station are given.

	IWC [kg m^{-3}]	Corresponding temperature [°C]	IWC [kg m^{-3}]	Corresponding temperature [°C]
	NSA		SGP	
absolute IWC$_{min}$	$4.07 \cdot 10^{-9}$	- 1.3	$1.10 \cdot 10^{-8}$	- 1.3
absolute IWC$_{max}$	$2.07 \cdot 10^{-4}$	- 5.4	$1.10 \cdot 10^{-3}$	- 4.2
absolute temp$_{min}$	$3.53 \cdot 10^{-6}$	- 29.3	$3.15 \cdot 10^{-6}$	- 34.1
absolute temp$_{max}$	$2.8 \cdot 10^{-7}$	- 0.2	$1.84 \cdot 10^{-7}$	- 0.8

	IWC [kg m^{-3}]	Temperature interval [°C]	IWC [kg m^{-3}]	Temperature interval [°C]
	NSA		SGP	
mean IWC $_{min}$	$4.97 \cdot 10^{-6}$	[- 10; - 5]	$3.09 \cdot 10^{-6}$	[- 5; 0]
mean IWC$_{max}$	$2.24 \cdot 10^{-5}$	[- 15; - 10]	$3.87 \cdot 10^{-5}$	[- 35; - 30]
median IWC$_{min}$	$3.16 \cdot 10^{-7}$	[- 10; - 5]	$4.04 \cdot 10^{-7}$	[- 5; 0]
median IWC$_{max}$	$6.00 \cdot 10^{-6}$	[- 15; - 10]	$2.23 \cdot 10^{-5}$	[- 25; - 20]
SD IWC$_{min}$	$1.11 \cdot 10^{-5}$	[- 25; - 20]	$1.75 \cdot 10^{-5}$	[- 30; - 25]
SD IWC$_{max}$	$3.66 \cdot 10^{-5}$	[- 15; - 10]	$5.43 \cdot 10^{-5}$	[- 15; - 10]
(IWC$_{mean}$-IWC$_{median}$)$_{min}$	$2.16 \cdot 10^{-6}$	[- 25; 20]	$2.69 \cdot 10^{-6}$	[- 5; 0]
(IWC$_{mean}$-IWC$_{median}$)$_{max}$	$1.64 \cdot 10^{-5}$	[- 15; - 10]	$1.95 \cdot 10^{-5}$	[- 15; - 10]

Table 6.2: This table shows the respective minima (*min*) and maxima (*max*) for NSA and SGP. The *absolute IWC* provides the absolute minimum and maximum of the ice water content with the corresponding temperature. The absolute temperature (*absolute temp*) represents the temperature range of the observed cloud cases to the corresponding station. In addition, the temperature intervals for the minimum and maximum values of mean, median, and standard deviation (SD) of the IWC are presented. The (IWC$_{mean}$-IWC$_{median}$) shows for each station the maximum and minimum difference between mean and median.

Statistic with HSRL

	cloud profiles [10^3]	Temperature [°C]	amount [%]
NSA$_{withHSRL}$			
total	642.2	–	–
min	0.4	- 37.5	0.07
max	160.5	- 7.5	25.0

Table 6.3: Table of the cases, which were determined using the algorithm presented in Chapter 3. Presented are the total number of cases observed at NSA with HSRL (*total*), the temperature interval with the fewest cases (*min*) and with the maximum cases (*max*). The associated percentages are given with respect to the *total* amount of cloud profiles at NSA.

	IWC $[\mathrm{kg\,m^{-3}}]$	Corresponding temperature [°C]	IWC $[\mathrm{kg\,m^{-3}}]$	Corresponding temperature [°C]
	$\mathrm{NSA}_{withCEIL}$		$\mathrm{NSA}_{withHSRL}$	
absolute IWC_{min}	$4.07 \cdot 10^{-9}$	- 1.3	$4.07 \cdot 10^{-9}$	- 0.7
absolute IWC_{max}	$2.07 \cdot 10^{-4}$	- 5.4	$2.09 \cdot 10^{-4}$	- 5.6
absolute temp_{min}	$3.53 \cdot 10^{-6}$	- 29.3	$7.81 \cdot 10^{-6}$	- 40.0
absolute temp_{max}	$2.8 \cdot 10^{-7}$	- 0.2	$2.80 \cdot 10^{-7}$	- 0.01

	IWC $[\mathrm{kg\,m^{-3}}]$	Temperature interval [°C]	IWC $[\mathrm{kg\,m^{-3}}]$	Temperature interval [°C]
	$\mathrm{NSA}_{withCEIL}$		$\mathrm{NSA}_{withHSRL}$	
mean IWC $_{min}$	$4.97 \cdot 10^{-6}$	[- 10; - 5]	$3.00 \cdot 10^{-6}$	[- 10; - 5]
mean IWC_{max}	$2.24 \cdot 10^{-5}$	[- 15; - 10]	$2.12 \cdot 10^{-5}$	[- 15; - 10]
median IWC_{min}	$3.16 \cdot 10^{-7}$	[- 10; - 5]	$2.53 \cdot 10^{-7}$	[- 5; 0]
median IWC_{max}	$6.00 \cdot 10^{-6}$	[- 15; - 10]	$1.86 \cdot 10^{-5}$	[- 35; - 30]
SD IWC_{min}	$1.11 \cdot 10^{-5}$	[- 25; - 20]	$7.49 \cdot 10^{-6}$	[- 40; - 35]
SD IWC_{max}	$3.66 \cdot 10^{-5}$	[- 15; - 10]	$3.57 \cdot 10^{-5}$	[- 15; - 10]
$(\mathrm{IWC}_{mean}\text{-}\mathrm{IWC}_{median})_{min}$	$2.16 \cdot 10^{-6}$	[- 25; 20]	$3.27 \cdot 10^{-6}$	[- 35; - 30]
$(\mathrm{IWC}_{mean}\text{-}\mathrm{IWC}_{median})_{max}$	$1.64 \cdot 10^{-5}$	[- 15; - 10]	$1.58 \cdot 10^{-5}$	[- 15; - 10]

Table 6.4: This table shows the respective minima (min) and maxima (max) for $\mathrm{NSA}_{withCEIL}$ and $\mathrm{NSA}_{withHSRL}$. The *absolute IWC* provides the absolute minimum and maximum of the ice water content with the corresponding temperature. The absolute temperature (*absolute temp*) represents the temperature range of the observed cloud cases to the corresponding instrument. In addition, the temperature intervals for the minimum and maximum values of mean, median, and standard deviation (SD) of the IWC are presented. The (IWC_{mean}-IWC_{median}) shows for each station the maximum and minimum difference between mean and median.

Declaration of Authorship

I declare that I have authored this thesis independently, that I have not used other than the declared sources / resources, and that I have explicitly marked all material which has been quoted either literally or by content from the used sources.

Furthermore, I certify that this research thesis or any part of it has not been previously submitted for a degree or any other qualification at the University of Leipzig or any other institution in Germany or abroad.

Leipzig, 26 January 2016

Franziska Hellmuth